Evolution of the Kangmar Dome, southern Tibet: Structural, petrologic, and thermochronologic constraints

Jeffrey Lee
Central Washington University, jeff@geology.cwu.edu

Bradley R. Hacker
University of California - Santa Barbara

William S. Dinklage
University of California - Santa Barbara

Yu Wang
State Seismological Bureau, Beijing

Phillip Gans
University of California - Santa Barbara

See next page for additional authors

Recommended Citation

Authors
Jeffrey Lee, Bradley R. Hacker, William S. Dinklage, Yu Wang, Phillip Gans, Andrew Calvert, JingLin Wan, Wenji Chen, Ann E. Blythe, and William McClelland

Evolution of the Kangmar Dome, southern Tibet: Structural, petrologic, and thermochronologic constraints

Jeffrey Lee[1,2], Bradley R. Hacker[3], William S. Dinklage[3,4], Yu Wang[5], Phillip Gans[3], Andrew Calvert[3], JingLin Wan[5], Wenji Chen[5,6], Ann E. Blythe[7], and William McClelland[8]

Abstract. Structural, thermobarometric, and thermochronologic investigations of the Kangmar Dome, southern Tibet, suggest that both extensional and contractional deformational histories are preserved within the dome. The dome is cored by an orthogneiss which is mantled by staurolite + kyanite zone metasedimentary rocks; metamorphic grade dies out up section and is defined by a series of concentric kyanite-in, staurolite-in, garnet-in, and chloritoid-in isograds. Three major deformational events, two older penetrative events and a younger doming event, are preserved. The oldest event, D1, resulted in approximately E-W trending tight to isoclinal folds of bedding with an associated moderately to steeply north dipping axial planar foliation, S1. The second event, D2, resulted in a high strain mylonitic foliation, S2, which defines the domal structure, and an associated approximately N-S trending stretching and mineral alignment lineation. Shear sense during formation of S2 varied from dominantly top S shear on the south dipping flank of the dome to top N shear on the north dipping flank. The central part of the dome exhibits either opposing shear sense indicators or symmetric fabrics. Microtextural relations indicate that peak metamorphism occurred post-D1 and pre- to early D2 deformation. Quantitative thermobarometry yields peak metamorphic conditions of ~445°C and 370 MPa in garnet zone rocks, increasing to 625°C and 860 MPa in staurolite + kyanite zone rocks. Pressures and temperatures increase with depth and northward within a single structural horizon across the dome and the apparent gradient in pressure is ~20% of the expected gradient, suggesting that the rocks were subvertically shortened after the pressure gradient was frozen in. Mica $^{40}Ar/^{39}Ar$ thermochronology yields 15.24 ± 0.05 to 10.94 ± 0.30 Ma cooling ages that increase with depth and young northward within a single structural horizon across the dome. Diffusion modeling of potassium feldspar $^{40}Ar/^{39}Ar$ spectra yield rapid cooling rates (~10-30°C/Myr) between ~11.5 and 10 Ma and apatite fission track ages range from 7.9 ± 3.0 to 4.1 ± 1.9 Ma, with a mean age of ~5.5 Ma. Both data sets show symmetric cooling across the dome between ~11 and 5.5 Ma. The S2 mylonitic foliation, peak metamorphic isobars and isotherms, and mica $^{40}Ar/^{39}Ar$ isochrons are domed, whereas potassium feldspar $^{40}Ar/^{39}Ar$ and apatite fission track isochrons are not, suggesting that doming occurred at ~11 Ma. Our data do not support simple, end-member metamorphic core complex-type extension, diapirism, or duplex models for gneiss dome formation. Rather, we suggest that the formation of extensional fabrics occurred within a zone of coaxial strain in the root zone of the Southern Tibetan Detachment System (STDS), implying that normal slip along the STDS and extensional fabrics within the Kangmar Dome were the result of gravitational collapse of overthickened crust. Subsequent doming during the middle Miocene is attributed to thrusting upward and southward over a north dipping ramp above cold Tethyan sediments. Middle Miocene thrust faulting in the Kangmar Dome region is synchronous with continued normal slip along the STDS and thrust motion along the Renbu Zedong thrust fault, suggesting that extension and contraction was occurring simultaneously within southern Tibet.

1. Introduction

The Himalayan orogeny records the Eocene-Recent continental collision between India and Asia, yet extension has been an important component in its evolution. Pliocene to Recent N-S striking grabens [*Armijo et al.*, 1986] appear to be the result of gravitational collapse of overthickened crust and high elevations within the Tibetan Plateau [*England and Houseman*, 1989; *Molnar and Tapponnier*, 1975, 1978]. Older extensional structures, also attributed to gravitational collapse, include the early to middle Miocene north dipping, low-angle Southern Tibetan Detachment System (STDS) [*Burchfiel et al.*, 1992; *Burg and Chen*, 1984; *Hodges et al.*, 1992] and two middle to late Miocene gneiss domes interpreted to be similar to metamorphic core complexes of the western United States [*Chen et al.*, 1990; *Pan and Kidd*, 1992].

The Kangmar dome is one of a series of such gneiss domes, the north Himalayan gneiss domes, which lie within the Tethys Himalaya south of the Indus-Tsangpo Suture Zone (ITSZ) and north of the STDS (Figure 1) and crop out within the axis of the north Himalayan antiform [*Hauck et al.*, 1998]. Gneiss domes are found in orogenic belts worldwide and are typically composed of a core of granitic migmatites or gneisses structurally overlain by a mantle of high-grade metasedimentary rocks [e.g., *Eskola*, 1949]. The origin of gneiss domes is a world-class problem and is typically attributed to three processes: diapirism

Figure 1. Regional tectonic map of the central Himalaya orogen after *Burchfiel et al.* [1992] and *Burg et al.* [1984] showing the location of the Kangmar Dome. GKT, Gyirong-Kangmar thrust fault system; ITSZ, Indus-Tsangpo Suture Zone; KK, Khula Kangri; MBT, Main Boundary Thrust; MCT, Main Central Thrust; STDS, Southern Tibetan Detachment System; WL, Wagye La; YCS; Yadong cross structure. Thrust fault is represented by teeth on the hanging wall; normal fault is represented by solid circle on the hanging wall. Inset, modified from *Burchfiel et al.* [1992] and *Tapponnier et al.* [1982], shows location of regional tectonic map.

[e.g., *Ramberg*, 1980], crustal shortening [e.g., *Brun*, 1983; *Ramsay*, 1967], or crustal extension [e.g., *Brun and Van Den Driessche*, 1994; *Miller et al.*, 1992]. Each of these processes has been proposed to be the mechanism by which the north Himalayan gneiss domes were formed and each has distinctly different implications for the tectonic evolution of southern Tibet and the high Himalaya.

Le Fort [1986] and *Le Fort et al.* [1987] suggested a diapiric origin for the north Himalayan domes, whereby thrusting along the Main Central Thrust (MCT) of hot portions of the Tibetan Slab over weakly metamorphosed sediments resulted in large-scale release of fluids that rose above the MCT and induced anatexis. The doming was suggested to result from compressive-stress-induced undulations enhanced by the buoyancy of anatectic melts [*Le Fort*, 1986; *Le Fort et al.*, 1987]. *Harrison et al.* [1997], on the basis of numerical simulations, suggested that the leucogranites exposed within these domes were also the products of anatexis caused by heat generated owing to shear stress along the Himalayan decollement. They implied that these magmas were hot enough and therefore sufficiently buoyant to rise diapirically into the middle crust.

In contrast, *Burg et al.* [1984] argued that the Kangmar Dome, one of the north Himalayan gneiss domes (Figure 1), is the result of purely contractional deformation and formed by a thrust duplex at depth; they based their conclusions on reconnaissance observations of south verging tight to isoclinal folds in the upper part of the metasedimentary carapace, the reorientation of fold axes to a N-S orientation in the lower part of the carapace, and increasing shear strain with structural depth. More recent reconnaissance studies in the Kangmar Dome [*Chen et al.*, 1990] documented a top-to-the-north mylonitic fabric in the high-grade metasedimentary rocks and in the orthogneiss. In addition, *Chen et al.* [1990] interpreted the contact between the orthogneiss core and metasedimentary mantle as an extensional detachment fault, similar to those associated with metamorphic core complexes of the western United States, and argued that displacement along the Kangmar detachment was northward, the same as the STDS. They concluded that like the STDS, the Kangmar Dome is an extensional feature that formed in response to gravitational collapse of the Himalayan topographic front.

The timing of events in the Kangmar dome is poorly known. The $^{40}Ar/^{39}Ar$ thermochronology on biotite and muscovite from

the orthogneiss yielded ages of 20.4 ± 0.6 and 17.3 ± 0.5 Ma, respectively, and from the high-grade schists yielded younger ages of 13.5 ± 0.6 and 13.0 ± 0.5 Ma, respectively [Maluski et al., 1988]. Maluski et al. [1988] interpreted these ages as cooling below ~335°-370°C at ~13-20 Ma, following emplacement of plutons during the middle Miocene. An alternative interpretation, suggested, but not favored, by Chen et al. [1990], is that the difference in mica ages across the detachment fault arose because the orthogneiss and metasedimentary rocks had different cooling histories following peak metamorphism but similar histories after juxtaposition across the detachment fault.

In the ideal end-member setting each of these models make specific and testable predictions about the nature of the contact between the metasedimentary mantle and the orthogneissic core, the geometry and kinematics of penetrative structures within the core and cover of high-grade metasedimentary rocks, the structural style in surrounding lower-grade rocks, the relation between metamorphism, magmatism, and deformation, and the three-dimensional cooling history. To test these predictions, this paper presents the results of new detailed geologic mapping, structural, kinematic, quantitative thermobarometric, and thermochronologic studies in the Kangmar Dome, southern Tibet, an area previously studied in reconnaissance by Burg et al. [1984] and Chen et al. [1990]. Our new detailed investigations show that the Kangmar gneiss dome resulted from both contractional and extensional deformation.

2. Regional Setting

The north Himalayan gneiss domes are exposed within the Tethys Himalaya, approximately halfway between the ITSZ to the north and the STDS to the south (Figure 1). This region is underlain by a miogeoclinal sedimentary sequence deposited on the passive northern margin of the India continent. The marine sediments are nearly continuous in age from Cambrian to Eocene [Gansser, 1964; Le Fort, 1975], with the Eocene marine sedimentary rocks probably marking an upper bound on the timing of the India-Asia continental collision. The zone is structurally complex, exhibiting Cretaceous to Holocene contractional and extensional structures in a variety of orientations [e.g., Le Fort, 1975; Searle, 1983; Armijo et al., 1986; Burg and Chen, 1984; Ratschbacher et al., 1994; Yin et al., 1994; Quidelleur et al., 1997]. The oldest structures are south directed thrust and fold nappes of Late Cretaceous and Paleocene age that are probably related to northward obduction. Younger structures, Eocene to Miocene in age, include shallow-dipping south directed thrust faults and steeply dipping north directed backthrust faults [Burg and Chen, 1984; Searle et al., 1988; Yin et al., 1994; Quidelleur et al., 1997]. Imbrication of the Tethys Himalaya is thought to be Miocene [Ratschbacher et al., 1994]. Pliocene to Recent N–S striking grabens [e.g., Armijo et al., 1986] appear to be the result of gravitational collapse of overthickened crust and high elevations. The E–W direction of extension is attributed to eastward extrusion along the Pacific margin [e.g., Molnar and Lyon-Caen, 1989; Molnar and Tapponnier, 1975, 1978; Tapponnier et al., 1982] and has been linked to the abrupt increase in surface elevation of the plateau as a consequence of convective removal of the lower continental lithosphere and the inception of gravitational collapse [e.g., England and Molnar, 1993].

The Kangmar Dome, located north of the Yadong cross structure, is one of the easternmost of the north Himalayan gneiss domes and, unlike the other domes, its elliptical map pattern trends N-S (Figure 1).

3. Geology of the Kangmar Dome

The Kangmar Dome is cored by an 11 km x 7 km K-feldspar + 2-mica-bearing augen gneiss mantled by Carboniferous to Triassic sedimentary rocks that range from staurolite-kyanite zone at the base to unmetamorphosed at the top (Plate 1 and Figure 2). The orthogneiss contains a well-developed LS fabric; the lineation is defined by elongate feldspar and quartz grains and stringers and aggregates of biotite or feldspar, and the foliation is defined by aligned biotite and muscovite and weakly flattened quartz grains. K-feldspar augen are typically 4-5 mm but up to 1 cm across and commonly have well-developed recrystallized tails forming σ-type or φ-type mantled porphyroclasts [Passchier and Simpson, 1986]. The orthogneiss has been intruded by few penetratively deformed, thin (a few meters wide) hornblende + plagioclase ± epidote metabasite dikes and fine-grained aplite dikes of unknown age.

Two orthogneiss samples processed for U-Pb geochronology yielded concordant and discordant multigrain and single grain zircon analyses (Figures 3 and 4 and Table 1) (supporting uranium-lead analytical data is provided in Table 2)[1]. Two abraded clear euhedral single zircons from sample KD100, collected from the structurally highest portion of the orthogneiss, yielded concordant and barely concordant analyses. Other fractions from this sample produced discordant results with the most discordant analysis derived from euhedral opaque zircon. The analyses fit a chord with upper and lower concordia intercepts of 509 ± 6 and 48 ± 47 Ma, respectively. An emplacement age of 508 ± 1 Ma is interpreted for this sample on the basis of the concordant single zircon analysis, and the observed discordance is attributed to Pb loss during Tertiary metamorphism and deformation. Sample KD101, collected from the structurally lowest portion of the orthogneiss, yielded similar results except no concordant analyses were obtained. In addition, fraction d, consisting of subhedral zircons versus euhedral grains comprising all other fractions, suggests that there is an inherited component, at least in portions of the zircon population. This observation is supported by partial dissolution results, which indicate the presence of both Pb loss effects and inherited xenocrystic components. Excluding fraction d, the conventional analyses define a line with an upper concordia intercept of 509 ± 18, Ma which is coincident with the age determined for sample KD100. Accordingly, samples KD100 and KD101 are interpreted to be similar in age, and an emplacement age of ~508 Ma is inferred for sample KD101. The emplacement ages determined during this study differ from the age of 562 ± 4 Ma on the basis of a concordant single zircon analysis reported for an orthogneiss sample within the Kangmar dome by Shärer et al. [1986]. This age difference may be due to the presence of multiple intrusive phases within the Kangmar dome, or the single grain analyzed by Shärer et al. [1986] may represent an inherited grain within a younger (508 Ma) intrusion.
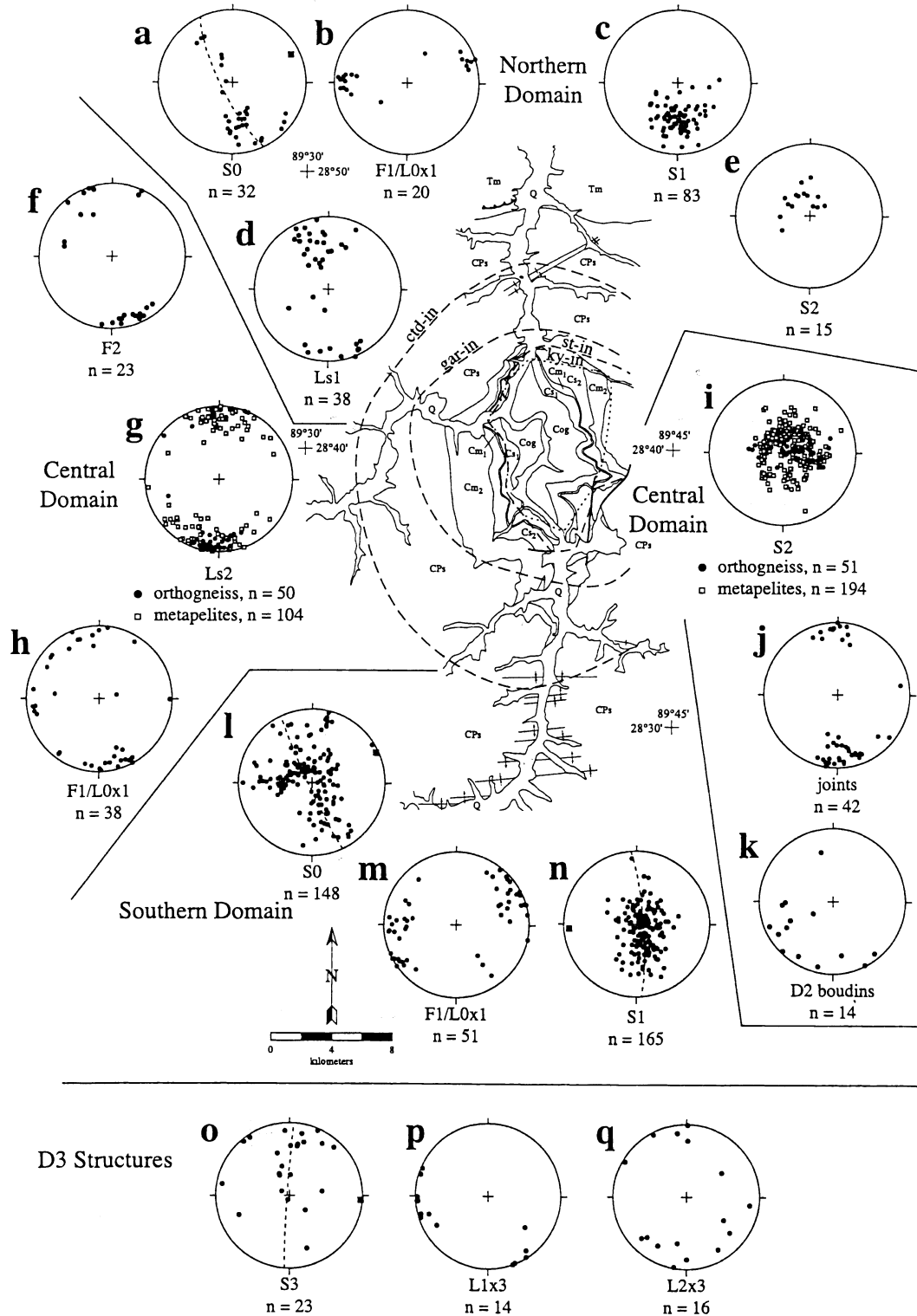
Figure 2. Simplified geologic map of the Kangmar Dome showing structural domains and metamorphic isograds. Structural data are plotted on lower hemisphere, equal area projections; number of measurements is indicated. In the northern domain, (a) poles to bedding, (b) F1 fold axes and L0x1 intersection lineations, (c) poles to S1 foliation, (d) Ls1 stretching lineations, and (e) poles to S2 foliation. In the central domain, (f) F2 fold axes, (g) Ls2 stretching lineations (orthogneiss is represented by solid circles; metapelite is represented by open squares), (h) F1 fold axes and L0x1 intersection lineations, (i) poles to S2 mylonitic foliation (orthogneiss is represented by solid circles; metapelite is represented by open squares), (j) poles to joints, and (k) boudin axes. In the southern domain, (l) poles to bedding, (m) F1 fold axes and L0x1 intersection lineations, and (n) poles to S1 foliation. D3 structures, (o) poles to S3 axial surface, (p) L1x3 intersection lineations, and (q) L2x3 intersection lineations. Dashed line and solid square in Figures 2a, 2l, 2n, and 2o are a best fit girdle to planar data and calculated fold axis, respectively. Here ctd-in, chloritoid isograd; gar-in, garnet isograd; st-in, staurolite isograd; ky-in, kyanite isograd.
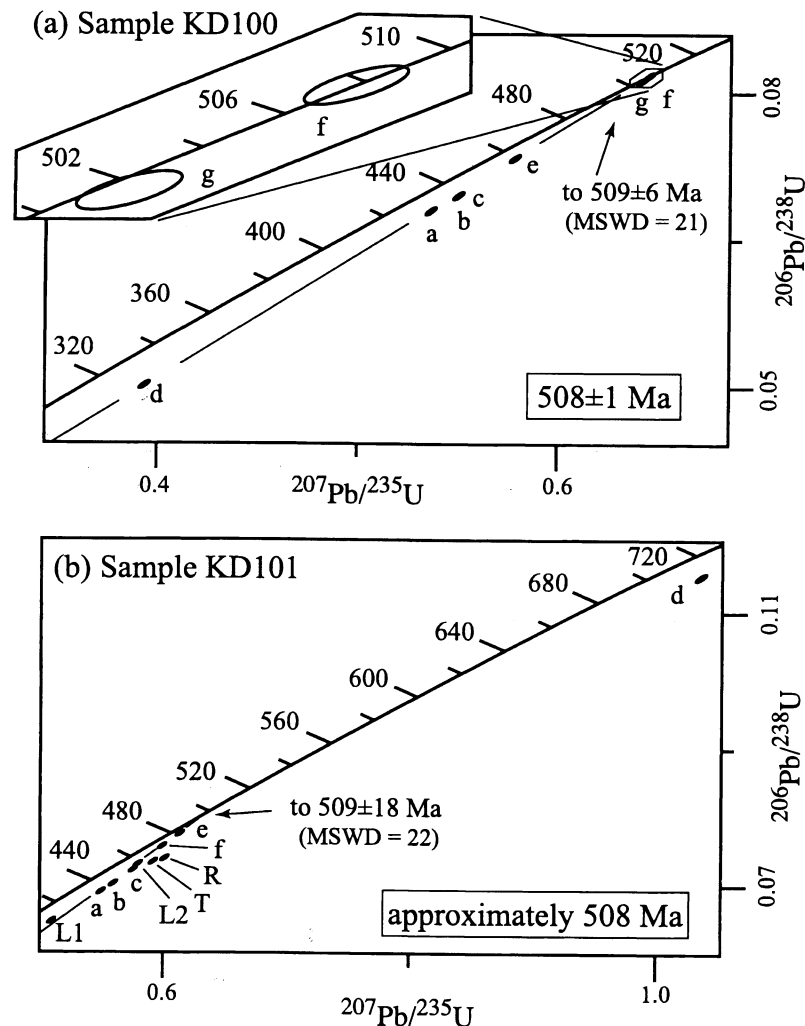
Figure 3. U/Pb concordia plot showing 17 analyses from two samples of the Kangmar orthogneiss. (a) Sample KD100, collected from the structurally highest part of the orthogneiss, yielding an interpreted emplacement age of 508 ± 1 Ma. (b) Sample KD101, collected from the structurally lowest part of the orthogneiss, yielding an interpreted emplacement age of ~508 Ma. MSWD is mean standard weighted deviation. See Table 1 and Figure 4 for location of samples.

Structurally overlying the orthogneiss is a garnet + staurolite + kyanite porphyroblast-bearing biotite + muscovite schist, which we refer to as the lower schist, Cs_1 (Plate 1). This unit also contains a well-developed LS fabric; the foliation is defined by aligned micas, weakly flattened quartz grains, and mica and quartz segregations. Porphyroblasts are up to 3 cm across and have strain shadows of quartz, white mica, and biotite. Locally, thin (decimeters) calcite + phlogopite + quartz calcschists and well-banded (1-3 cm thick) tan to buff quartzite of polygonal equant quartz grains are interlayered with the schist. Locally, penetratively deformed, decimeters-wide metabasite dikes, consisting of hornblende + plagioclase ± epidote, are boudinaged within the schist. This unit, as well as the two overlying units (see below), have been assigned a Carboniferous age by *Chen et al.* [1990] because they are similar to fossil-bearing units elsewhere in the region.

Structurally above Cs_1 is a coarsely recrystallized tan to buff marble which locally contains phlogopite and biotite in thin, pe-

litic-rich layers. This unit contains a well-developed foliation but poorly developed stretching lineation. Locally exposed within this unit are boudinaged penetratively deformed hornblende + plagioclase + epidote ± pyroxene ± chlorite ± Fe-oxide-bearing metabasite dikes. This unit, informally called the lower marble, Cm_1, pinches out to the south (Plates 1 and 2).

Overlying Cm_1 is another schist unit, the upper schist, Cs_2 (Plate 1). Cs_2 is dominantly a coarse-grained garnet porphyroblast-bearing mica schist which locally contains staurolite and kyanite (Figure 2). Pale to medium gray micaceous metapsammite increases up section; mafic dikes are scarce. Cs_2 contains a well-developed LS fabric; foliation boudinage is common.

Cs_2 is in gradational contact with the overlying upper marble, Cm_2 (Plate 1). Cm_2 varies from a medium-grained buff, gray, to white marble that locally is phlogopite-bearing to a medium- to coarse-grained marble or beige, micaceous calc schist. Scarce crinoids are present. Mafic dikes are present and boudinaged
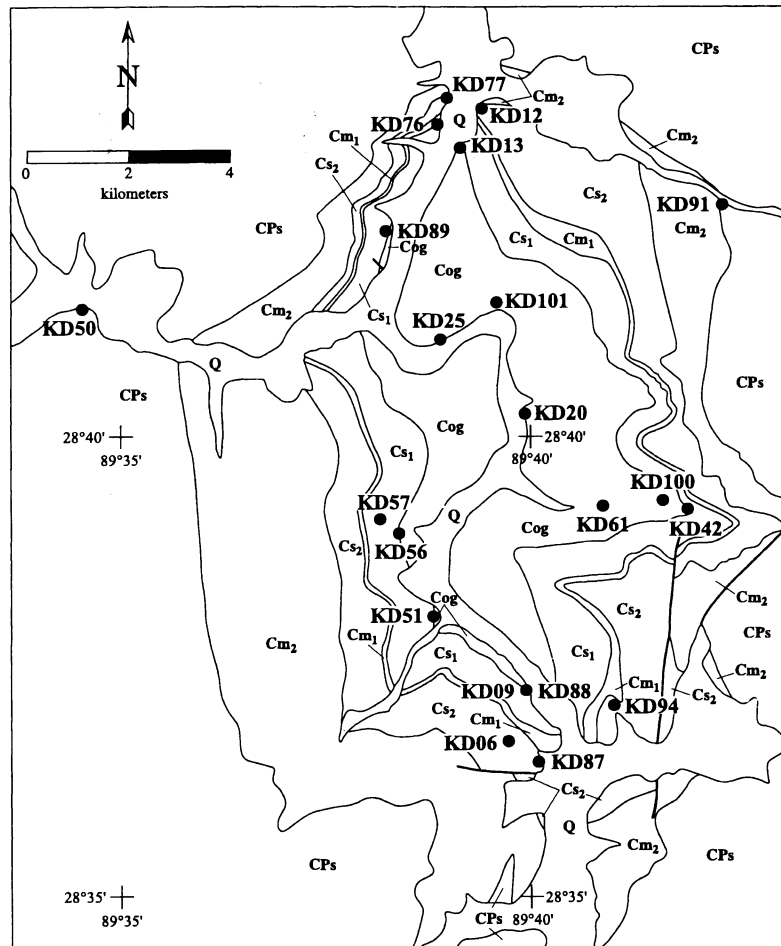
Figure 4. Simplified geologic map of the Kangmar Dome showing the location of samples collected for apatite fission thermochronology, $^{40}Ar/^{39}Ar$ thermochronology, quantitative thermobarometry, quartz c axis fabric studies, and U/Pb zircon geochronology. Table 1 lists the latitude, longitude, and elevation for each sample. In text and Table 1, letters appended to sample numbers represent separate samples collected at that locality, e.g., samples KD42B, KD42C, and KD42AA were collected at locality KD42.

within the dominant foliation but unlike the mafic dikes at lower structural levels, these dikes are not penetratively deformed. Marbles high in this unit contain the Carboniferous Orthotichia-Wilkingia fossil assemblage [*Liang and Wang*, 1983].

A dominantly sandstone and shale unit, CPs, overlies Cm_2. The base of this unit is within the garnet and chloritoid zone, whereas the top of the unit is unmetamorphosed (Plate 1 and Figure 2). Exposed in the lower portion of CPs are typically brown, but also rust to tan, quartzite interlayered with locally graphitic garnet-bearing schists and chloritoid-bearing gray, brown, or tan phyllite. These rocks posses a fairly well-developed LS fabric; foliation boudinage is common. At higher structural levels the unit is composed of dominantly black argillite, carbonaceous meta-psammite, gray to green slate, and shale. At the highest structural levels, CPs consists of pink-tan weathering, massive to cross-bedded sandstone to orthoquartzite interlayered with lesser green-gray mudstone with limonite spots, and gray to buff mudstones and marls. The sandstone is typically 90-95% quartz with 5-10% feldspar and lithic fragments. This

mixed siliciclastic sequence has been assigned a Carboniferous-Permian age [*Chen et al.*, 1990].

Exposed at the highest structural levels mapped are unmetamorphosed sedimentary rocks of unit Tm. These rocks are well-bedded, interlayered light buff mudstone and siltstone; red-weathering pyrite-bearing sandstone; fine-grained argillaceous limestone and marl; cream weathering sericitic mudstones (up to 1 m thick); and buff limestone beds (up to 15 cm thick). This unit has been assigned a Triassic age [*Chen et al.*, 1990].

4. Structural Chronology

4.1. Introduction

On the basis of mapping and structural studies at 1:50,000 scale in the Kangmar Dome, we have identified two primary penetrative deformational events: (1) a first deformational event, D1, which horizontally shortened bedding into a series of asymmetric folds and (2) a second, superimposed high-strain

Table 1. Summary Data Table

Sample	Sample Location			Thermobarometry		U/Pb Zircon	$^{40}Ar/^{39}Ar$ Age, Ma		Apatite Fission
	Latitude, °N	Longitude, °E	Elevation, m	Pressure, MPa	Temperature, °C	Age, Ma	Muscovite	Biotite	Track Age, Ma
KD06	28°36.9'	89°40'	4530	660±60	536±39				
KD09C	28°37.3'	89°40'	4300				14.82±0.04[a]		
KD12B	28°43.6'	89°39.4'	4200	860±80	624±39				
KD12C	28°43.6'	89°39.4'	4200				12.23±0.03[b]	10.94±0.03[a]	
KD13B	28°43.2'	89°39.2'	4170					12.61±0.03[a]	4.1±1.9
KD20	28°40.3'	89°39.5'	4250				14.56±0.05[b]	16.28±0.04[a]	5.7±2.3
KD25[c]	28°41'	89°38.9'	4230						
KD42B	28°39.3'	89°42'	4700	860±60	614±30				
KD42C[c]	28°39.3'	89°42'	4700						
KD42AA	28°39.3'	89°42'	4700					13.66±0.03[a]	6.5±1.3
KD50	28°41.4'	89°34.5'	4270	370±60	446±44				
KD51B	28°38'	89°38.9'	4310	670±60	554±33				
KD56AA	28°39'	89°38.3'	4560					14.46±0.03[a]	4.6±3.4
KD56BB	28°39'	89°38.3'	4560				14.98±0.03[b]	14.91±0.03[a]	
KD57[d]	28°39.2'	89°38.1'	4700						
KD61	28°39.3'	89°40.9'	4480				15.24±0.05[b]	15.99±0.04[a]	7.9±3.0
KD76[d]	28°43.4'	89°38.8'	4230						
KD77	28°43.7'	89°38.9'	4230					11.82±0.03[a]	
KD87A[c]	28°36.5'	89°40.1'	4340						
KD87B	28°36.5'	89°40.1'	4340				13.35±0.03[a]	12.86±0.04[a]	
KD88B	28°37.3'	89°40'	4300				14.82±0.03[a]	17.04±0.04[a]	4.7±1.5
KD89	28°42'	89°38.1'	4470	680±70	564±38		12.71±0.04[b]	12.12±0.03[a]	
KD91	28°42.9'	89°42.4'	4430	830±70	562±35				
KD94[d]	28°37.5'	89°41'	4770						
KD100	28°39.4"	89°41.8'	4650			508±1			
KD101	28°41.5'	89°39.6'	4500			~508			

[a] Preferred age.
[b] Weighted mean plateau age.
[c] Hornblende $^{40}Ar/^{39}Ar$ geochronology sample.
[d] Quartz caxis fabric sample.

deformational event, D2, that vertically thinned and horizontally stretched the lower part of the structural sequence. These structural data define three structural domains: northern and southern domains dominated by D1 structural fabrics and a central deeper domain of high strain D2 structural fabrics (Figure 2). Microstructural textures indicate that peak metamorphism occurred pre- to early D2 deformation. Superimposed on D2 fabrics are weakly developed, low strain D3 fabrics, D4 doming, and brittle deformational structures.

4.2. D1 Deformation

The oldest event, D1, best exposed and dominant at the highest structural levels, folded bedding into map- to mesoscopic-scale, tight to isoclinal, NE trending, SE vergent folds, F1, associated with a moderately NW dipping axial planar foliation, S1 (Plates 1 and 2 and Figures 2a-2c and 2l-2n). Map-scale F1 folds are spectacularly exposed within Tm and the southernmost and northernmost exposures of CPs, where the long limbs dip moderately north and the short limbs dip steeply south. The S1 axial planar foliation is a fine-grained slaty cleavage at the highest structural levels in Tm but becomes more coarse grained and phyllitic in CPs, where it is defined by aligned fine-grained micas, flattened detrital quartz grains, and microlithons rich in mica or quartz. Locally, a NNW-SSE trending stretching lineation, Ls1, defined by aligned tabular chloritoid grains and strain shadows developed around them, is associated with the S1 foliation (Plate 1 and Figure 2d). The S1 foliation is often refracted between quartzites and phyllites, a geometry that is in part responsible for the girdle distribution of S1 axial planes plotted in Figures 2c and 2n.

4.3. D2 Deformation

A younger, high-strain deformational event, D2, is manifested at higher structural levels as a series of open to tight, recumbent, NNW-SSE trending folds of bedding and S1 with wavelengths of ≤0.5 m to tens of meters (Figure 2f). With increasing structural depth, bedding and the S1 foliation are first crenulated by a spaced (millimeter to centimeter spacing), subhorizontal S2 foliation and finally transposed parallel to a mylonitic S2 foliation. The S2 mylonitic foliation dips moderately to steeply north on the north flank and shallowly south on the south flank (Plates 1 and 2 and Figure 2i). Associated with the high-strain S2 foliation is an approximately N-S stretching lineation, Ls2, defined by strain shadows developed on metamorphic porphyroblasts; aligned biotite and muscovite aggregates; aligned prismatic minerals, such as staurolite, kyanite, and hornblende; quartz rods; K-feldspar ribbons and aggregates; and recrystallized tails on K-feldspar porphyroclasts (Figure 2g). Preservation of the S1 foliation within strain shadows where the S2 crenulation foliation is weak is uncommon. Quartz veins and metabasite dikes exposed within the schists and marbles are commonly boudinaged and pulled apart parallel to the Ls2 stretching lineation, yielding approximately SW trending boudin axes (Figure 2k).

Within both the northern and southern domains the mean trend of L0x1 intersection lineations and F1 fold hinges is approximately E-W, whereas in the central domain the mean trend is approximately N-S (Figure 2h). We interpret the shift in the approximately E-W trending mean lineation toward the approximately N-S trending Ls2 stretching lineation as the result of strain-related progressive rotation toward parallelism with the stretching lineation [e.g., *Sanderson*, 1973]. The difference in mean orientations of the L0x1 intersection lineations and F1 fold hinges from the northern and southern domains relative to the central domain is ~70°, indicating an X/Z strain ratio of at least 30. Even though the bulk X/Z finite strain appears to be ~30, the strain is not uniform across the dome. The high-grade metasedimentary rocks on the northern flank of the dome are ~40% as thick as those on the southern flank. We interpret this difference as indicating higher D2 strains in the northern flank of the dome, although we cannot rule out a northward decrease in thickness of sedimentary units.

Mesoscopic and microscopic structures within the orthogneiss and the overlying high-grade metasedimentary rocks, such as asymmetric boudins of metabasite dikes and quartz veins, shear bands, S/C fabrics, strain shadows on metamorphic porphyroblasts, tails on K-feldspar porphyroclasts, asymmetric grain shape foliations, and crystallographic preferred orientation (CPO) of quartz record the sense of shear associated with the development of the high strain S2 foliation. Asymmetric boudins of dikes and quartz veins are typically lozenge-shaped with comminuted tails that often lie at different elevations on both sides of the boudin or are stair-stepped. Late-stage shear bands dip more steeply than the mylonitic S2 foliation and are typically spaced up to 5-20 cm apart. S/C fabrics within the orthogneiss are, in general, poorly developed. Strain shadows on metamorphic porphyroblasts consisting of quartz, white mica, and biotite, are variably developed and range from symmetrically to asymmetrically disposed about the porphyroblast.

Recrystallized, granoblastic quartz grains exhibiting variably developed undulatory extinction typify quartz microtextures, although locally, quartz contains a weakly developed, dynamically recrystallized grain shape foliation that is oblique to S2. These observations suggest that the rate of diffusion-controlled recovery in quartz during D2 deformation was greater than the rate of work hardening associated with dislocation glide in that mineral. CPOs were measured on three quartzite samples distributed across the dome (Figures 4 and 5), in which quartz textures vary from straight boundaries in equigranular, granoblastic quartz grains developed in response to annealing to irregular grain boundaries formed in response to grain boundary migration recrystallization. Samples KD94 and KD57, located on the south and central part of the dome, respectively, exhibit type 1 girdle patterns [*Lister*, 1977], in which the fabric skeletons are symmetric with respect to the mylonitic foliation but the density distribution is asymmetric, indicating top-south and top-north sense of shear, respectively. Sample KD76, on the northern flank of the dome, shows a cleft girdle [*Lister and Hobbs*, 1980], in which the fabric skeleton is also symmetric with respect to the mylonitic foliation but the density distribution is asymmetric, indicating top-north sense of shear.

Kinematic fabrics exposed on the north and south flanks of the dome are dominated by top down to the north and top down to the south senses of shear, respectively (Plate 2). However, locally, both schist units exhibit scarce exposures of alternating horizons (at the decimeter to meter scale), exhibiting opposing sense of shear. The central part of the dome is characterized by coaxial fabrics, opposing shear sense within a single outcrop, or an absence of kinematic indicators (Plate 2). Although we could
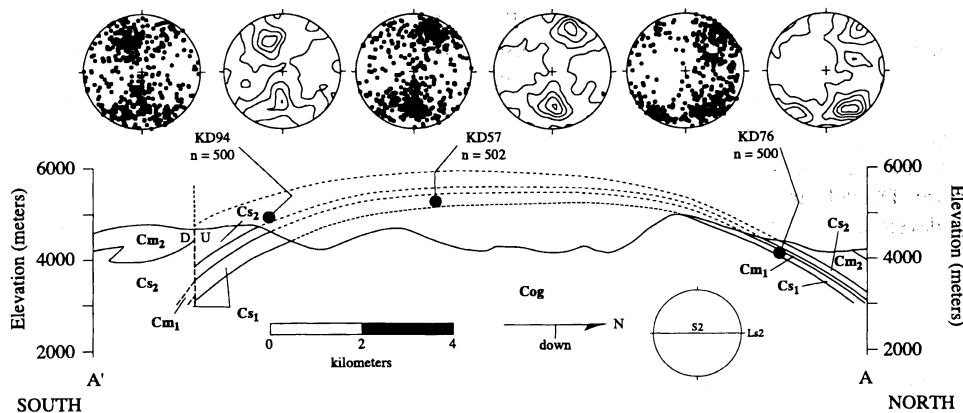
Figure 5. Quartz *c*axis fabrics of samples discussed in text projected into the central part of the N-S cross section (see Plate 2). Lower hemisphere, equal area projections, geographic orientation of stereonets, orientation of S2 and Ls2, and number of *c*axes measured are indicated. Contour intervals are 1, 2, 3, 4, and 5 times uniform distribution. See Table 1 and Figure 4 for location of samples.

not quantify the magnitude of shear strain, the bulk shear strain history appears to be coaxial to slightly noncoaxial with higher strains on the northern flank.

4.4. D3 Deformation

D3 deformational fabrics are weakly developed and are restricted to the metapelites of CPs and older units. D3 fabrics are characterized by a weak crenulation to kink folds, with half-wavelengths of millimeters to centimeters, of either the S2 or S1 foliation. The associated S3 axial planar surface strikes approximately E-W and dips moderately to steeply south but is not associated with the development of a penetrative axial planar fabric (Figure 2o); no consistent sense of asymmetry was observed. Intersection of S3 with the older planar foliations produces an intersection lineation: L1x3 trends approximately west and L2x3 trends approximately N-S (Figures 2p and 2q).

4.5. D4 Deformation

D4 doming folds the S2 mylonitic foliation, which best defines the dome, and the S3 axial planar surface (Plates 1 and 2 and Figures 2i and 2o). The S2 mylonitic foliation defines a 18 km x 9 km doubly plunging, N-S elongate antiformal dome that dips moderately to steeply north on the north flank, shallowly south on the south flank, and shallowly on the east and west flanks (Plates 1 and 2 and Figure 3i). On the north flank, doming steepened the north dipping S1 foliation, whereas on the south side, doming rotated the S1 foliation through horizontal to a moderately southward dip, forming a map-scale, approximately E-W trending D4 synform (Plates 1 and 2 and Figures 2c and 2n).

4.6. Brittle Structures

Abundant joints and scarce faults within the dome cut all older penetrative fabrics. E-W striking, near-vertical joints (Figure 2j) are well developed within the orthogneiss. These joints developed orthogonal to Ls2, suggesting a genetic link between the two fabrics. Faults are few in number, ranging from a small offset (tens of meters), poorly exposed north dipping thrust fault at high structural levels at the northern end of the map area within

Tm to three poorly exposed, variably striking, near-vertical faults in the central part of the dome (Plate 1).

The contact between the orthogneiss core and metasedimentary mantle has been interpreted as either a metamorphic core complex-type detachment fault [*Chen et al.*, 1990], an unconformity [*Burg et al.*, 1984; *Zhang et al.*, 1986], or an intrusive contact [*Hayden*, 1912; *Zhou et al.*, 1981]. On the basis of our observations across the entire dome this contact ranges from a knife-sharp, concordant contact with no mesoscopic evidence of brittle deformation to a locally discordant contact between the S2 in the orthogneiss and S2 in the overlying schist with up to 1 m of fault gouge and breccia developed only within crushed and sheared schist overlying the orthogneiss. We attribute this local deformation to the rheologic contrast between the schist and orthogneiss because there is no evidence for structural omission across this contact. The $^{40}Ar/^{39}Ar$ thermochronology (see below) supports this field interpretation. On the basis of our field observations, $^{40}Ar/^{39}Ar$ thermochronology, and U/Pb geochronology we interpret this contact as a nonconformity along which there has been minimal brittle motion.

5. Metamorphic History

Petrographic examination of tens of thin sections from pelitic samples revealed a clear prograde sequence of mineral assemblages that define a series of isograds that increase in grade toward the orthogneiss (Figure 2). The lowest grade is marked by diagenetic fabrics, fossils, and neocrystallized chlorite. At deeper levels, chlorite is joined by biotite and chloritoid, defining the chloritoid zone. The breakdown of chloritoid, accompanied by increasing Mg content in biotite, led to the growth of garnet; the garnet-in and chloritoid-out isograds coincide closely at the resolution of our sample spacing. At higher temperatures, garnet + chlorite assemblages reacted to form staurolite + biotite parageneses. Staurolite is joined by kyanite in the highest temperature rocks. The breakdown of staurolite or kyanite was not observed nor was the growth of sillimanite. This, along with arguments presented below, implies that the orthogneiss in the core of the
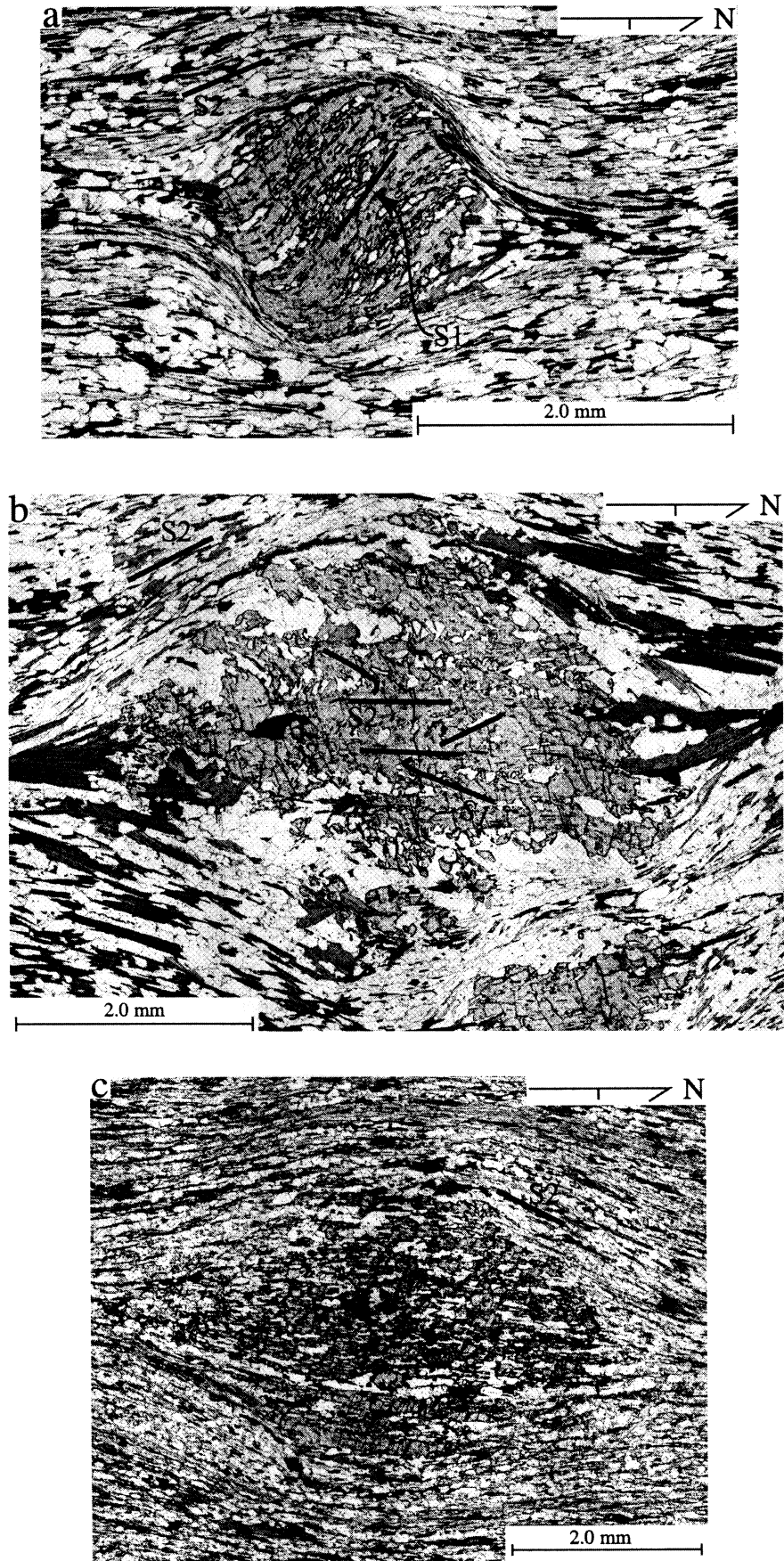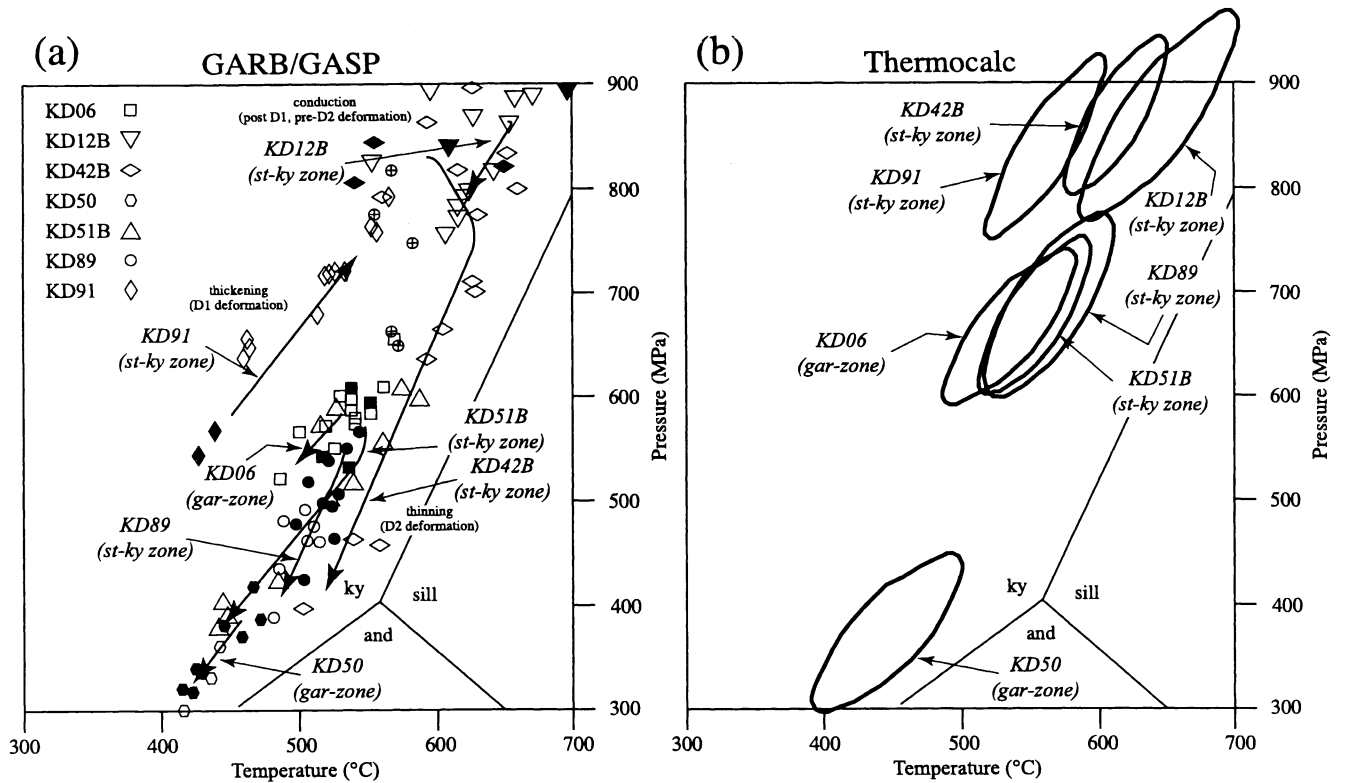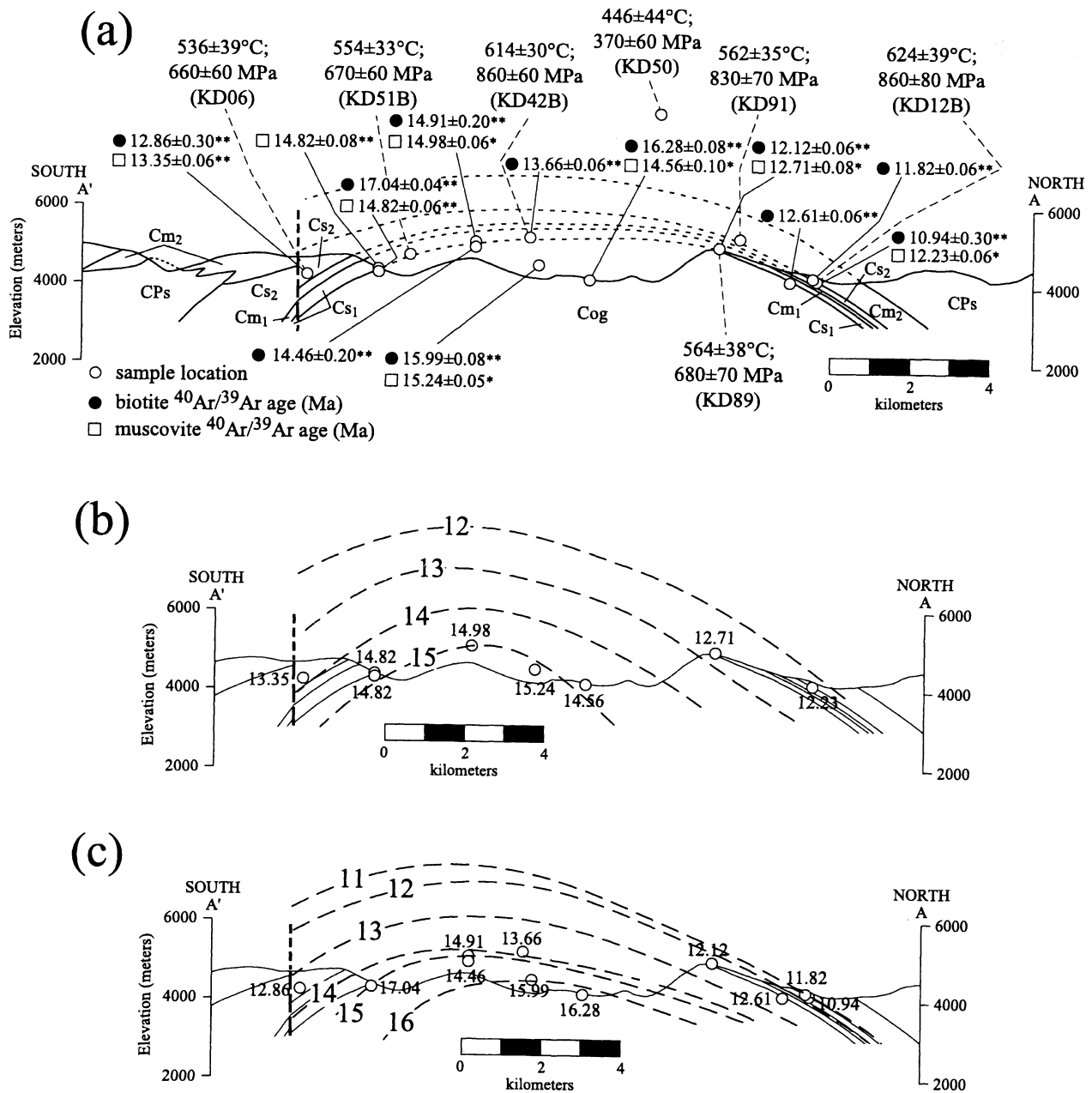
Figure 6.

Figure 7. PT diagrams showing the results of thermobarometry analyses of pelites. (a) Garnet-biotite (GARB) temperatures and garnet-kyanite-quartz-plagioclase (GASP) pressures. Mineral rims are given by open symbols; mineral cores are given by solid symbols with crosses; mineral inclusions are given by solid symbols. PT paths inferred from variation in rim pressures and temperatures are illustrated as solid lines. (b) Peak temperatures and pressures calculated from Thermocalc. Ellipses represent weighted mean temperatures and pressures for rim compositions for each sample. Here and, andalusite; gar, garnet; ky, kyanite; sill, sillimanite; st, staurolite. Aluminosilicate stability fields are from *Bohlen et al.* [1991]. Peak PT conditions calculated from Thermocalc are projected on a N-S cross section in Figure 8; sample locations are shown in Table 1 and Figure 4.

dome was not the heat source for the metamorphism. If it were, higher temperatures should have been attained. The isograds are roughly concentric to the domal structure defined by the warped stratigraphy overlying the orthogneiss. However, in detail, the garnet–in, staurolite–in, and kyanite–in isograds cut across mapped units and structures, defining a thermal high NE of the center of the dome, further evidence that the orthogneiss exposed in the core was not the heat source for metamorphism (Figure 2).

Microstructures reveal the relative age relations between the growth of metamorphic porphyroblasts and development of the

S1 and S2 foliations. (1) A garnet porphyroblast with a curved internal foliation, S1, defined by quartz, mica, and opaque mineral inclusion trails, is truncated by the external foliation, S2, defined by mica and quartz. The external S2 foliation wraps around the porphyroblast and forms strain shadows, indicating that D2 deformation continued after growth of the porphyroblast (Figure 6a). (2) A garnet porphyroblast with an internal foliation of crenulated quartz and opaque mineral inclusion trails that we interpret as preserved S1 foliation crenulated by S2, has the external foliation, S2, wrapped around it, forming strain shadows (Figure

Figure 6. Photomicrographs of schist units showing microstructural relations between metamorphic porphyroblasts, external foliation, and internal foliation. (a) Garnet growth pretectonic to syntectonic with early D2 deformation, as shown in this strongly deformed Cs_2 schist. This photomicrograph shows a garnet porphyroblast (center) with an internal inclusion trail, defined by quartz and opaque minerals, that is straight in the center of the porphyroblast, curved within the rim, and truncated by the external foliation. Asymmetric strain shadows of quartz and mica indicate top-south sense of shear. (b) Strongly deformed Cs_1 schist showing a large garnet porphyroblast (center) with an internal foliation of crenulated quartz and opaque inclusion trails that we interpret as preserved S1 foliation crenulated by S2 foliation. The external mylonitic foliation, S2, of quartz and mica wraps around the porphyroblast, indicating that D2 deformation continued after garnet growth ceased. Asymmetric strain shadows of quartz and mica indicate top-north sense of shear. (c) Strongly deformed CPs schist showing a garnet porphyroblast (center) with inclusion trails that are curved and continuous with the external foliation, S2, indicating syntectonic growth. Photomicrographs are plane light; geographic orientation is indicated.
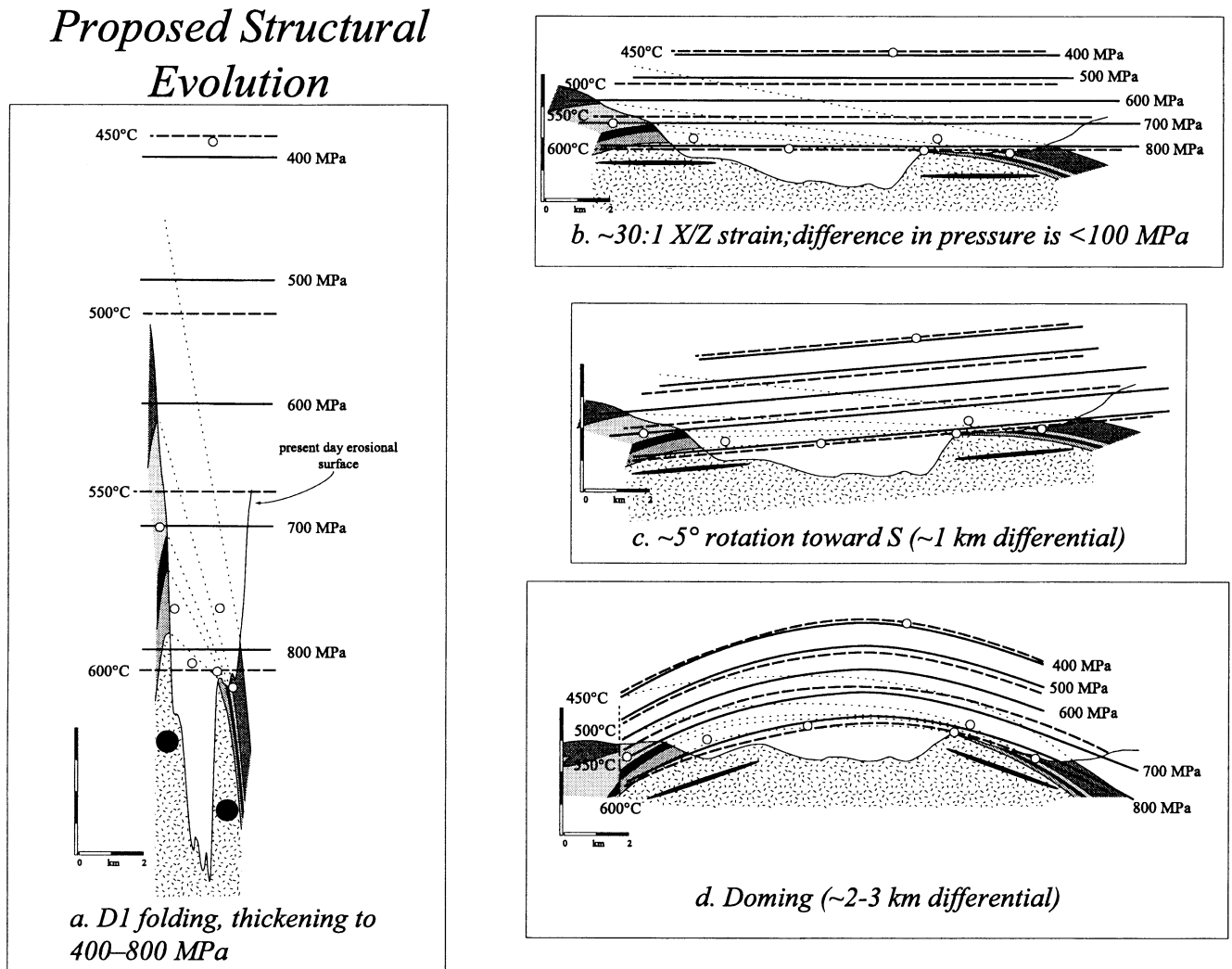
Figure 8. (a) Thermobarometric, based on Thermocalc, and mica $^{40}Ar/^{39}Ar$ geochronology results projected onto the central part of the N-S cross section (see Plate 1). Thermobarometric sample numbers are in parenthesis. Ages are given in Ma and errors are 1 sigma; weighted mean plateau ages are indicated by asterisks; preferred ages are indicated by double asterisks. See Figures 10 and 11 for age spectra. (b) Isochrons of muscovite $^{40}Ar/^{39}Ar$ plateau and preferred ages projected on the central part of the N-S cross section. (c) Isochrons of biotite $^{40}Ar/^{39}Ar$ preferred ages projected on the central part of the N-S cross section.

6b). (3) A garnet porphyroblast contains slightly curved inclusion trails defined by quartz that are continuous with the external foliation, S2 (Figure 6c). These microstructures, in particular those exhibited in Figure 6b, indicate the following chronology of events: (1) development of S1 during D1 deformation, (2) crenulation of S1 by S2 during the early stages of D2 deformation, (3) growth of index metamorphic minerals over D2 crenulated inclusion trails, and (4) development of a mylonitic S2 foliation that wraps around the metamorphic porphyroblasts during continued D2 deformation.

Six samples were examined in considerable detail for quantitative thermobarometry. Each sample was examined carefully with backscattered electron imaging to identify mineral assemblages and reaction textures. Qualitative element concentration maps (Fe, Mn, Mg, Ca, and Na) were made by X-ray imaging garnet, biotite, muscovite, and plagioclase; three to

Proposed Structural Evolution

a. D1 folding, thickening to 400–800 MPa

b. ~30:1 X/Z strain; difference in pressure is <100 MPa

c. ~5° rotation toward S (~1 km differential)

d. Doming (~2-3 km differential)

Figure 9. Proposed structural evolution for the Kangmar Dome. (a) D1 folding and thickening leads to peak pressures of 400-800 MPa recorded in the rocks. (b) D2 vertical thinning and horizontal stretching of the previously thickened rocks, which thins the section to ~20% of its pre-D2 thickness. (c) Rotation of the Kangmar area ~5° to the south. (d) Present-day geometry of structures, peak isotherms, and peak isobars. Open circles are samples analyzed for quantitative thermobarometry; thick dashed lines are isotherms; thick solid lines are isobars; solid ellipses are schematic strain markers.

five crystals of each were mapped in each sample. A quantitative wavelength-dispersive line scan of each mapped garnet was then made to assess elemental zoning. Quantitative line scans were also made for three to five contiguous garnet–biotite pairs and spatially associated muscovite and plagioclase.

Garnet morphologies and zoning types vary systematically across the Kangmar Dome. Garnets in the chloritoid zone have complex shapes, suggesting "rapid" growth and low importance of interfacial free energies, whereas garnets in higher-rank samples are subhedral to anhedral. Major elements show prograde zoning profiles in chloritoid zone garnets, with bell-shaped Mn, decreasing Ca, and increasing Mg and Fe from core to rim. Garnets from garnet zone rocks are similar but show flattened Mn and Fe profiles, suggesting diffusional modification. Staurolite–kyanite zone garnets show similarly modified profiles

plus a reversal (increase) in Mn concentration at the rim indicative of minor garnet resorption.

Pressures and temperatures were calculated using Thermocalc [*Holland and Powell*, 1998] (1998 database), garnet–biotite (GARB) thermometry [*Ferry and Spear*, 1978; *Hodges and Spear*, 1982], garnet–kyanite–quartz-plagioclase (GASP) equilibria [*Ghent*, 1976; *Ghent et al.*, 1979], and garnet–biotite–muscovite–plagioclase (GMBP) equilibria [*Ghent and Stout*, 1981]; garnet activities were modeled after *Ganguly et al.* [1996], plagioclase activities were modeled after *Elkins and Grove* [1990], and mica activities were modeled after *Hodges and Spear* [1982]. The results are exhibited in Figure 7, where rims of minerals in contact are summarized as solid lines, and in Figure 8a and Table 1, where rim conditions determined using Thermocalc are indicated (supporting mineral compositions and

calculated pressures and temperatures are provided in Table 3). Rather than assume that all mineral pairs within a single sample should yield the same calculated PT conditions, we expect that different pairs closed to diffusion at different times, leading to a range of PT conditions for a single sample. These data imply a clockwise PT path of the sort produced by crustal thickening, thermal conduction, and crustal thinning (Figure 7a) [e.g., *Thompson and England*, 1984]. Calculated peak temperatures and pressures range from ~446°C and 370 MPa in the garnet zone to~624°C and 860 MPa in the staurolite + kyanite zone (Figures 7b and 8a).

What are the spatial relationships among the calculated pressures and temperatures, and how do they compare to the geologic structure? Regardless of whether one chooses peak temperatures or final temperatures, apparent isotherms can be drawn that increase with structural depth and increase northward within a given structural horizon (Figures 8a and 9d), yielding a metamorphic field gradient of ~45°C/km. Pressures, both peak and final, also increase northward within a given structural horizon, such that it is impossible to draw apparent isobars that do not cut across the structure (Figure 9d). There are three salient observations that fall from the PT data. First, the presence of pressures of 400–800 MPa suggests that these rocks were thickened or buried for such pressures to have been obtained. This is consistent with microtextural relations that show growth of peak index minerals after D1 folding. Second, the apparent gradient in pressure is ~140 MPa/km, well in excess of the expected gradient of 27 MPa/km for supracrustal rocks with an average density of 2700 kg/m^3. The development of such a subvertically foreshortened pressure gradient requires a factor of about five subhorizontal stretching after the pressure gradient was "frozen in." Third, the PT data from the deepest samples, KD12 and KD91, indicate an average thermal gradient throughout the crust of ~20°C/km prior to thinning, whereas data from the shallowest sample, KD50, indicate a gradient of ~30°C/km. Such gradients are typical of Barrovian metamorphism resulting from crustal thickening and are incompatible with metamorphism in a magmatic arc. In addition, there is no field evidence for a magmatic heat source, although such a source could be just below the present level of exposure. However, if metamorphism was the result of advection, it would have been coincidental that the heat source was emplaced immediately after thickening.

6. Thermochronology

The ^{40}Ar/^{39}Ar and fission track thermochronology was completed to characterize the exhumation history of the high-grade rocks within the Kangmar Dome. Three hornblende, 20 mica, and six potassium feldspar samples collected from metabasite dikes and mylonitized rocks of the orthogneiss core and schist units within the metasedimentary cover were analyzed for ^{40}Ar/^{39}Ar thermochronology. Six apatite samples collected from the orthogneiss core were analyzed for fission track thermochronology. These samples were selected to provide age constraints on metamorphism and cooling histories across the dome parallel to the stretching lineation and across the orthogneiss/lower schist contact.

The ^{40}Ar/^{39}Ar thermochronology age of a sample is interpreted as the time at which the sample cooled below the closure temperature [*Dodson*, 1973]. For relatively rapid cooling rates the estimated closure temperatures are estimated at 535°±50°C (hornblende) [*Harrison*, 1981], 370°±50°C (muscovite) [*Lister and Baldwin*, 1996], and 335°±50°C (biotite) [*Grove and Harrison*, 1996; *Harrison et al.*, 1985]. Weighted mean plateau ages (WMPA) are reported where >50% of the ^{39}Ar released in contiguous steps is within 1σ error. For disturbed spectra, preferred ages (PA) are reported where the spectrum is relatively flat but does not meet the strict criterion for a WMPA.

The fission track "age" of a sample is commonly interpreted as the time at which the sample cooled below the closure temperature and is determined by measuring the density of fission tracks and the U concentration of the sample [*Naeser*, 1976]. At a cooling rate of ~10°C/Myr, the closure temperature for preservation of fission tracks in F-rich apatites (95% of apatites) is ~120°C [e.g., *Naeser*, 1979].

Analytical techniques, results of argon isotopic analyses, and fission track analyses are provided in Tables 4 and 5, age spectra and apatite ages are shown in Figures 10-12, and ages are projected onto a N-S cross section in Figures 8 and 12. Sample localities are shown in Figure 4 and sample localities and summary ages are given in Table 1.

6.1. Hornblende

Three hornblende samples from penetratively deformed metabasite dikes were analyzed to provide an age estimate of the peak of metamorphism. All three samples yield highly disturbed age spectra with double gradient type patterns and are uninterpretable (Figure 10). Total gas ages range from 27.36 to 51.16 Ma, and isochron analysis does not reveal a simple nonatmospheric trapped component to explain these complex spectra.

6.2. White Mica

Eight white mica samples from the orthogneiss core and overlying schists were analyzed. Five of the samples yield well-behaved plateaus, and three yield disturbed age spectra with interpretable ages (Figure 10). White mica ages increase down structural section from 12.23 ± 0.06 to 15.24 ± 0.05 Ma and increase southward within a given structural horizon across the dome (Figure 8b).

6.3. Biotite

Twelve biotite samples from the orthogneiss core and overlying schists were analyzed. Most of these samples yield disturbed spectra, although a couple yield near plateaus. All but three biotite samples yield interpreted ages that are younger than coexisting muscovite (Figures 8 and 11), providing confidence that these ages are meaningful. Like the white micas, biotite ages increase down structural section from 10.94 ± 0.30 to 16.28 ± 0.08 Ma and increase southward within a given structural horizon across the dome (Figure 8c). Muscovite and biotite ages from the same sample provide an estimate of the rate of cooling from ~370° to 335°C; calculated cooling rates are high varying from ~25° to ~70°C/Myr.

6.4. Potassium Feldspar

Six potassium feldspar samples from the orthogneiss core were analyzed over 66-72 steps (Figure 12). All six samples yield age spectra with old apparent ages over the first 2-10% of
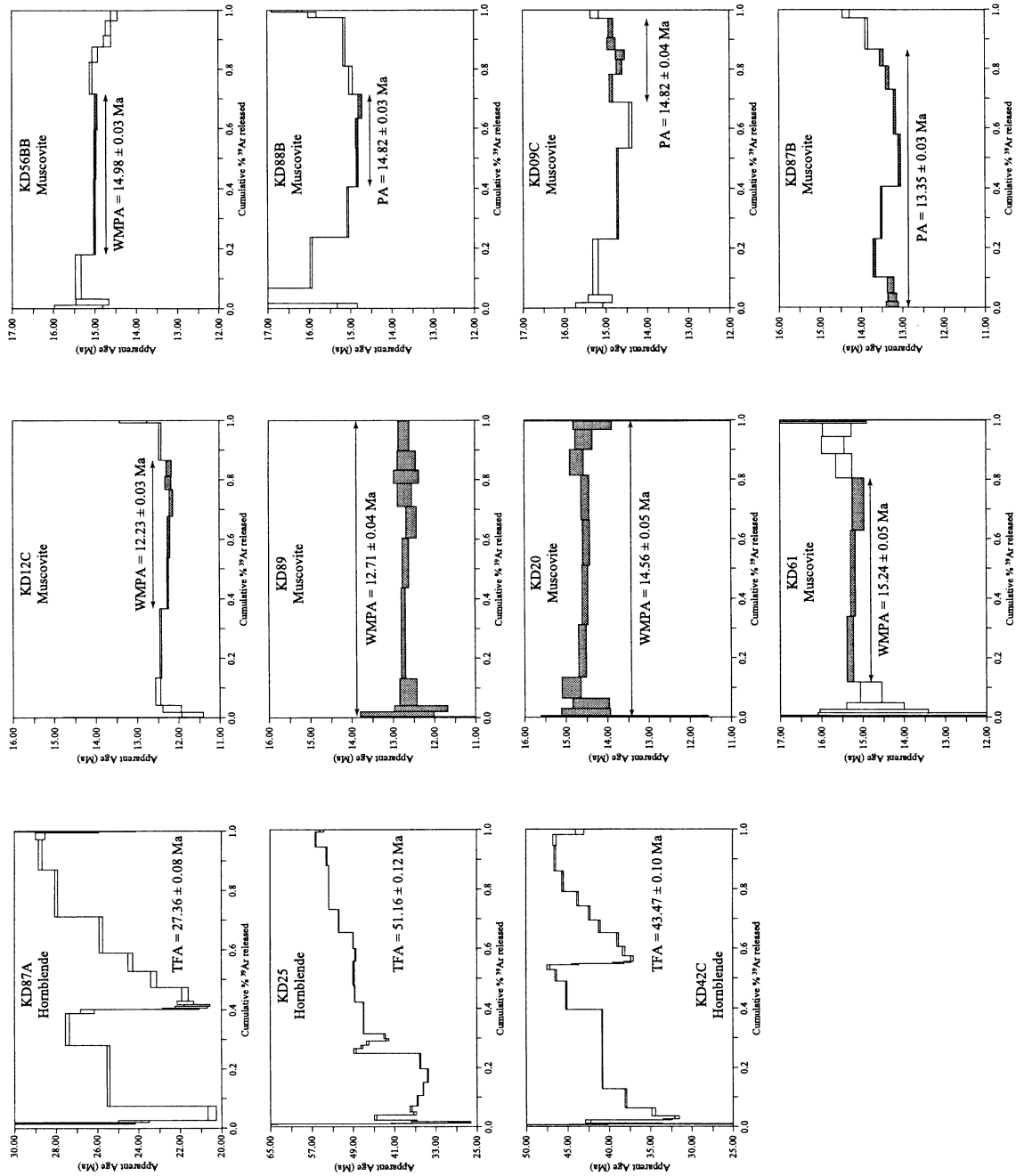
Figure 10. Hornblende and muscovite $^{40}Ar/^{39}Ar$ age spectra. Shaded steps are those used in determining the weighted mean plateau age (WMPA) or preferred age (PA). Samples with WMPA or PA ages are projected onto the central part of the NS-cross section in Figure 8. TFA is total fusion age.
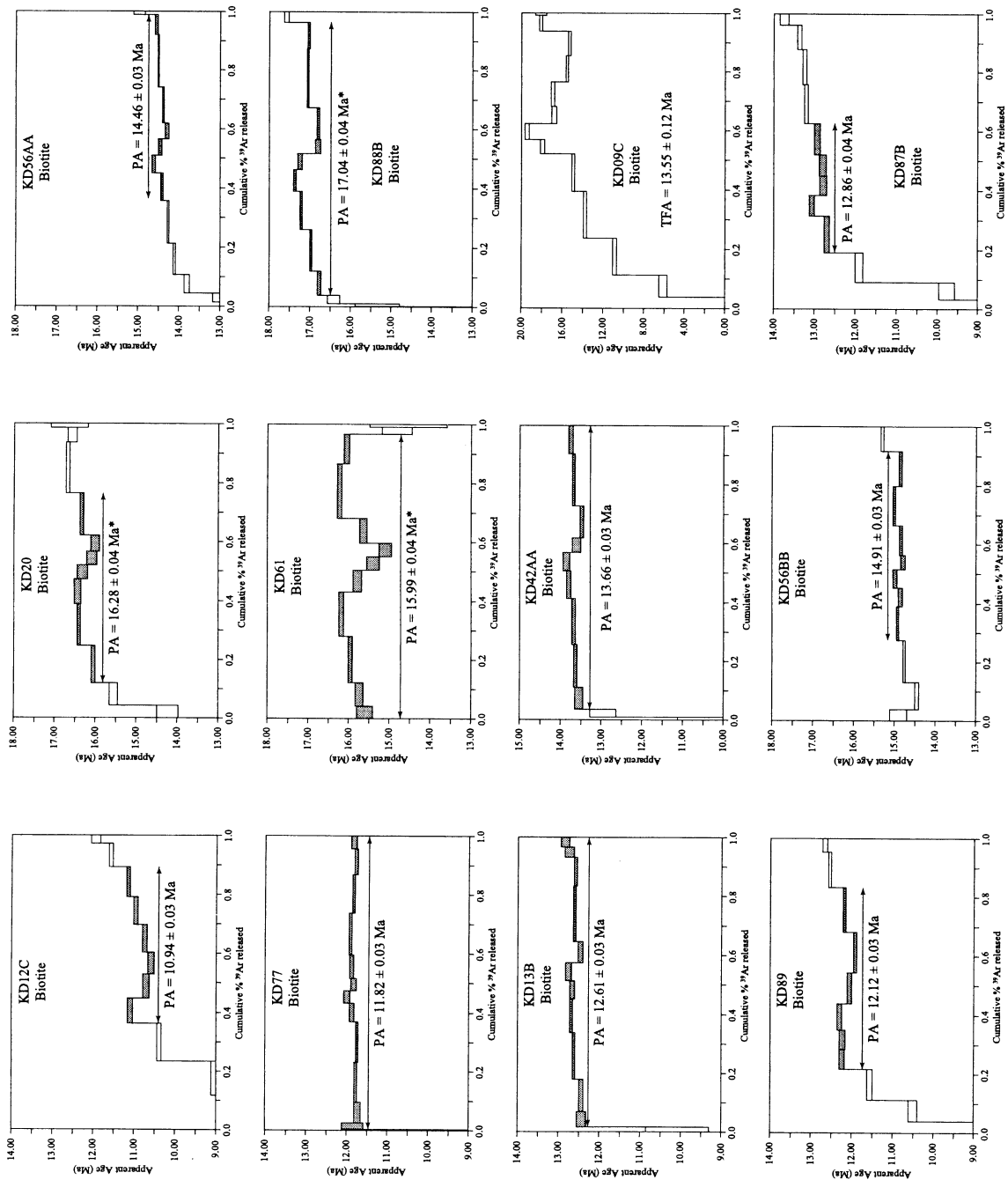
Figure 11. Biotite $^{40}Ar/^{39}Ar$ age spectra. Shaded steps are those used in determining the PA. Samples with PA ages are projected onto the central part of the N-S cross section in Figure 8. Asterisks represent biotite age older than coexisting muscovite age; TFA is total fusion age.
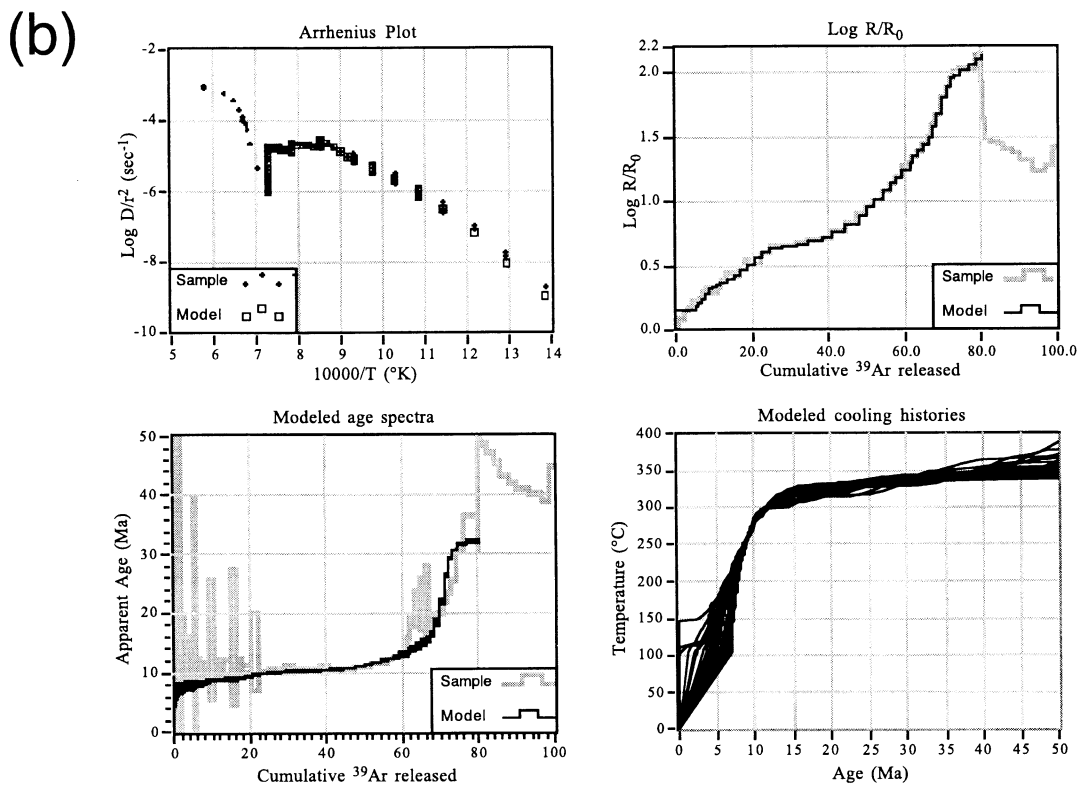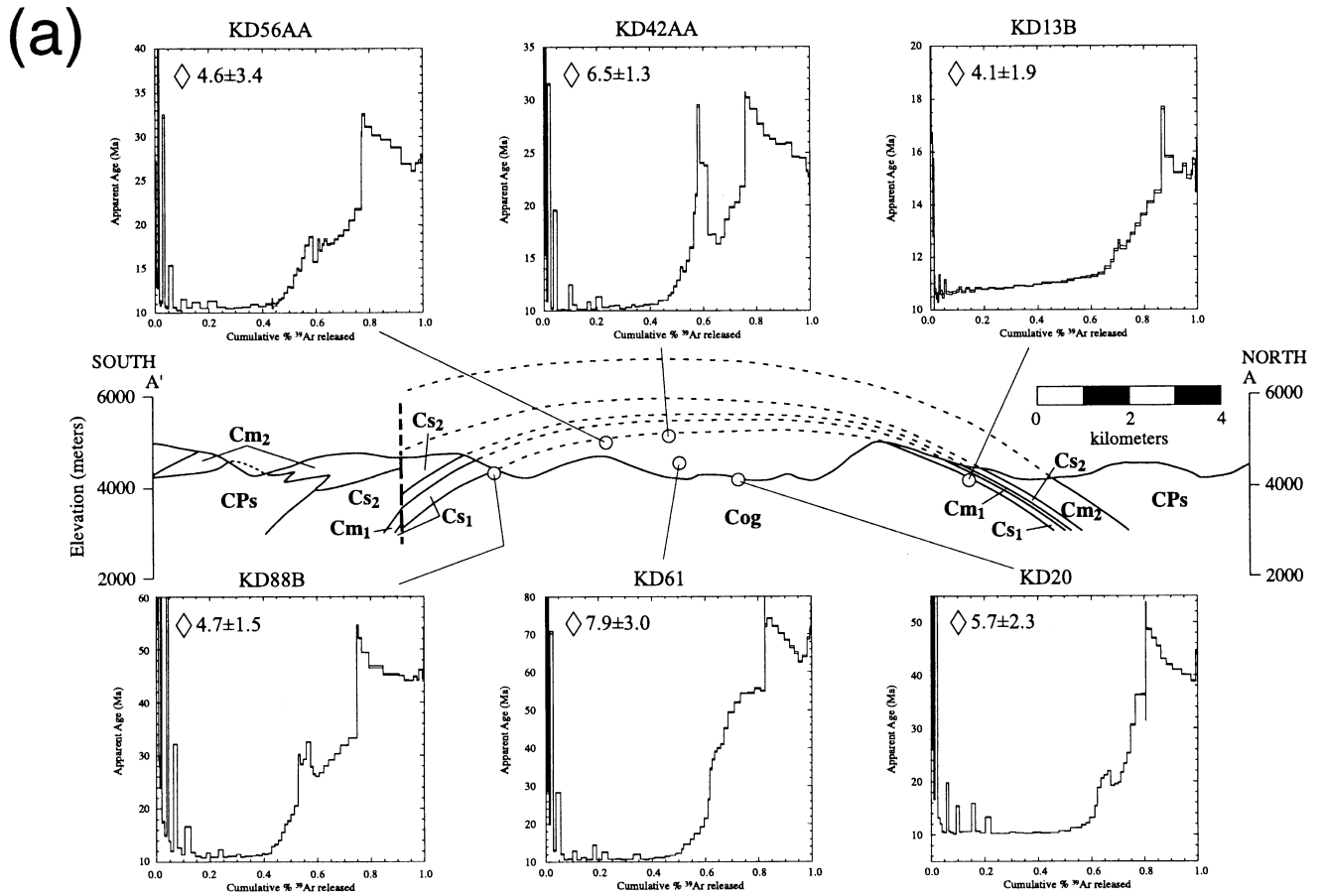
Figure 12. (a) Potassium feldspar ^{40}Ar/^{39}Ar age spectra and apatite fission track ages (open diamonds) projected onto the central part of the N-S cross section (see Plate 2). (b) Example of diffusion domain modeling showing Arrhenius plot, log R/R_0 plot, release spectra, and range of cooling histories for sample KD20.

[39]Ar released indicating incorporation of excess argon. This is followed by ages that climb slowly from 10 to 11 Ma over the next ~5-45% of [39]Ar released. The exception is sample KD13B, in which ages climb slowly from 10.5 to 11.5 Ma over the next 2-65% [39]Ar released. Over the last 40-60% gas released, all six samples exhibit complex age spectra characterized by ages that climb steeply and erratically, defining double-gradient-type patterns indicating incorporation of excess argon; ages as old as 45-70 Ma occur at the high temperature steps. Diffusion modeling of the potassium feldspar spectra, based on the theory of *Lovera et al.* [1989], provide an estimate of the middle- to low-temperature cooling histories across the dome. Because excess argon was incorporated over the first 2-10% and the last 40-50% of [39]Ar released, only the flat portion of the spectra (5-60% of [39]Ar released) was modeled. Modeling yields reasonably good fits to the Arrhenius data and good fits between observed and modeled log R/R_0 and age spectrum plots (Figure 12b). Eight domains produced the best fit, and calculated domain diffusion parameters, activation energy E and frequency factor D_0/r^2, range from 44.39 to 48.8 kcal/mol and 4.742 to 6.252/s, respectively. The calculated cooling histories show that the orthogneiss cooled quickly (~10°-30°C/Myr) from as high as ~350° to as low as ~250°C between 11.5 and 10.0 Ma, thus indicating that the dome cooled symmetrically at this time.

6.5. Apatite

Six apatite separates from the same rock samples that provided the potassium feldspar separates, were analyzed to provide constraints on the low-temperature exhumation history (Figure 12a). The fission track ages for the six samples ranged from 4.1 ± 1.9 to 7.9 ± 3.0 Ma; all ages are central ages [*Galbraith and Laslett,* 1993] with 1σ error. The errors are large on these ages because the apatites had relatively low concentrations of U. In addition, sample KD61 appeared to have at least two separate apatite populations, with ages of 7.9 and 13.9 Ma. However, because of the difficulty in analyzing this sample (there were numerous inclusions within the apatites) as well as the [40]Ar/[39]Ar thermochronometric data from this sample we are using only the younger age in our interpretations. The six fission track ages overlap at 1σ error, indicating that the dome symmetrically cooled through ~120°C at 5.5 Ma, the mean age for all samples. The cooling rate between coexisting muscovite [40]Ar/[39]Ar ages and apatite fission track ages is rapid at ~25°-30°C/Myr, consistent with the calculated potassium feldspar cooling histories.

There are five notable observations that fall from the thermochronology data. First, mica ages increase down structural section (Figures 8b and 8c) reflecting either compositional variation (i.e., higher closer temperatures) with depth, incorporation of excess argon at higher temperatures, or cooling from below due to underthrusting of a cold slab. Because there is no correlation between Mg number and biotite or muscovite age, it seems unlikely that compositional variation can explain the increase in mica ages down section. Furthermore, muscovites from the deepest exposures in the dome yield plateau ages of 15.27 ± 0.05 and 14.56 ± 0.05 Ma, suggesting that incorporation of excess argon at higher temperatures also cannot explain the increase in mica ages. Biotite from these samples, however, yield ages older than the coexisting muscovite (Figures 8, 10, and 11), implying that these samples have incorporated excess argon, although biotite from higher structural levels do not. Therefore the most plausible explanation for the observation that mica ages increase with

depth is refrigeration from underthrusting of a cold slab. If this interpretation is correct, our thermochronology data do not corroborate the suggestion of *Maluski et al.* [1988] that cooling within the Kangmar Dome followed emplacement of plutons. Second, mica ages young northward within a given structural horizon (Figures 8b and 8c), suggesting that either the north flank of the dome resided at slightly deeper structural levels before exhumation or there was a greater degree of reheating on this flank of the dome. We favor the former interpretation because it is most compatible with the northward increase in peak metamorphic pressures and temperatures within a given structural horizon and because there is no field or metamorphic evidence for middle Miocene magmatic activity in this dome. Accordingly, if we assume subhorizontal isotherms, this relation implies that exhumation at the northern end of the dome through the 370° to 335°C isotherms occurred 2-3 Myr after the southern flank of the dome. Implicit in this interpretation is that the rocks were tilted northward and exhumed southward. Third, there is no discontinuity in mica ages across the contact between the orthogneiss and overlying schist, supporting our field interpretation that there is no structural omission across and little brittle motion along this contact. We cannot, however, rule out the possibility that the orthogneiss and metasedimentary rocks had different cooling histories following peak metamorphism but similar histories (i.e., cooling below ~370°-335°C) following juxtaposition due to faulting [e.g., *Chen et al.,* 1990]. Fourth, the uniform cooling histories derived from the potassium feldspar and apatite data suggest that the dome was symmetrically exhumed between ~11 and 5.5 Ma. Fifth, the cooling rate of ~25°-40°C/Myr, from the closure temperature for muscovite to the annealing temperature for apatite, appears to be relatively constant across the dome and reflects both refrigeration and exhumation.

7. Interpretation

7.1. Structural Evolution of the Kangmar Dome

The structural history and pressure-temperature conditions we have documented in the Kangmar Dome allow us to characterize the structural evolution of this gneiss dome (Figure 9). The key to this evolution is the apparent gradient in peak pressure, from garnet zone rocks to staurolite-kyanite zone rocks, of ~140 MPa/km. The development of such a subvertically shortened pressure gradient requires that these rocks were vertically thinned to ~20% of their original thickness after the pressure gradient was frozen in.

The data we have collected therefore lead to the following tectonic history (Figure 9). The miogeoclinal section exposed within the Kangmar Dome was thickened and buried by distributed folding during D1 deformation, such that garnet zone rocks were buried to ~15 km depth and staurolite-kyanite zone rocks, the bottom of the section, were buried to ~30 km depth (Figure 9a) (see also the thickening part of the PT path shown in Figure 7a). On the basis of microtextural relations, peak pressures were recorded in the rocks after D1 deformation and prior to or during the early stages of D2 deformation (conduction part of the PT path, Figure 7a). Following peak metamorphism, the rocks were subhorizontally stretched by a factor of about five, collapsing the apparent isobars to ~20% of their original thickness (Figure 9b) (thinning part of the PT path, Figure 7a). The resultant finite strain of ~30:1 (X/Z) is compatible with the development of the

mylonitic S2 foliation and N-S trending Ls2 stretching lineation and with the apparent ~70° rotation of the approximately E-W-trending F1 fold axes and L0x1 intersection lineations in the northern and southern domains to the nearly N-S trend in the central domain. The rocks were subsequently tilted southward ~5°; the northern end of the dome was lifted ~1 km relative to the southern end to account, at least in part, for the northward increasing gradient in pressure (Figure 9c). Recrystallized feldspar tails, the crystal-plastic behavior of quartz, and the new growth of biotite in strain shadows indicate metamorphism at amphibolite to upper greenschist facies conditions during mylonitic deformation. However, because temperature-controlled recovery processes in quartz outpaced the rate of work hardening associated with dislocation glide, temperatures must have remained high following D2 deformation. Finally, the core was domed 2-3 km upward relative to the outside to create the domal form (Figure 9d). The S2 foliation, isobars, isotherms, and mica $^{40}Ar/^{39}Ar$ isochrons are domed (Plate 2 and Figures 8 and 9) but potassium feldspar $^{40}Ar/^{39}Ar$ isochrons are not, implying that doming occurred at temperatures below the blocking temperature for biotite, ~335°C but above the modeled high-temperature, ~300°C, part of the cooling histories for the potassium feldspar samples. Doming occurred at ~11 Ma, the $^{40}Ar/^{39}Ar$ age of the youngest biotite and the age of symmetric cooling recorded in the potassium feldspar samples. Although we have no age constraint for the onset of D2 deformation, we believe that the structural evolution illustrated in Figures 9b-9d most likely occurred as a continuum closely spaced in time. If our inference is correct, then D2 deformation is early(?) to middle Miocene in age.

The above discussion is predicted on some important assumptions. We have assumed plane strain deformation, a sensible supposition given that D2 structures are characterized by well-developed L-S tectonites. In addition, we have assumed that the measured peak pressures were recorded in the rocks at the same time; if the section was thinned or thickened inhomogeneously, e.g., by faults cutting between different samples, this assumption is incorrect. There is, however, no field evidence that faults cut between different samples. Note that because metamorphic field gradients are defined by the spatial distribution of peak temperatures that generally occurred at different times, the apparent thermal gradient defined by the Kangmar Dome samples (~10°C/km; Figure 9a) has no simple relationship to thermal gradients that actually existed during the tectonic history.

In summary, our work has documented a first phase of deformation characterized by N-S contraction leading to thickening in the Kangmar Dome region followed by thermal reequilibration and peak metamorphism which, in turn, was followed by a second phase of deformation characterized by horizontal extension and vertical thinning and, finally, a third phase of deformation characterized by doming.

7.2. Mechanism of Gneiss Dome Formation

The origin of gneiss domes is typically attributed to three processes, metamorphic core complex-type extension, diapirism, or duplex formation, and each of these processes has been proposed as the mechanism by which the north Himalayan gneiss domes were formed. In an ideal end-member setting each of these hypotheses make specific and testable predictions about the following: (1) the nature of the contact between the orthogneiss and cover of high-grade metasedimentary rocks; (2) the structural and kinematic history of the high-grade rocks and surrounding

low grade rocks; (3) the temporal, spatial, and genetic relation between metamorphism, magmatism, and deformation; and (4) the cooling history.

Chen et al. [1990] first suggested that the Kangmar dome formed as a result of metamorphic core complex like extension. They based their model on top-north mylonitic fabrics in the high-grade metasedimentary rocks and orthogneiss and their interpretation that the contact between the orthogneiss core and metasedimentary cover was an extensional detachment fault. In addition, *Hauck et al.* [1998], on the basis of International Deep Profiling of Tibet and Himalaya (INDEPTH) seismic reflection data, suggested that the STDS resurfaces to the north as the contact between the orthogneiss and metasedimentary rocks in the Kangmar Dome. Our data, however, do not corroborate a metamorphic core complex-type mechanism for four salient reasons: an upper plate of weakly metamorphosed to unmetamorphosed rocks cut by imbricate normal faults is not present, our field observations along the contact between the orthogneiss and metasedimentary rocks are not compatible with a detachment fault, bulk shear strain appears to be coaxial, and mica $^{40}Ar/^{39}Ar$ cooling ages increase with depth.

A simple magmatic diapir also appears to be an unlikely mechanism because there is no field or petrologic evidence for a young plutonic body within or beneath the Kangmar Dome. However, on the basis of our field and structural data alone we cannot rule out the possibility that the country rocks were of low enough viscosity, such that relatively low density high-grade metamorphic to migmatitic rocks present just below current levels of exposure rose diapirically leading to vertical thinning, horizontal stretching, and the development of the domal form. However, because mica $^{40}Ar/^{39}Ar$ ages cooling ages increase with depth, implying that the high-grade rocks within the Kangmar Dome were cooled from below, this hypothesis is untenable.

Burg et al. [1984] interpreted the Kangmar domal form as the result of a south vergent thrust duplex. We did not, however, observe tilted horses and thrust faults sandwiched between flat-lying thrust faults above and below characteristic of simple duplexes. Nor did we observe an up dip sense of shear and cooling ages younging in the direction opposite the sense of shear. Therefore this end-member model also seems implausible.

In addition to the data we have collected from the Kangmar Dome, there are two important regional relations that bear on its development and its role in the tectonic evolution of southern Tibet (Figures 1 and 13). First, surface geologic mapping indicates that the Kangmar Dome lies in the hanging wall of the north-dipping Gyirong-Kangmar thrust (GKT) fault system (Figures 1 and 13) [*Burg and Chen*, 1984; *Ratschbacher et al.*, 1994; *Wu et al.*, 1998; *J. Lee, W. Dinklage, Y. Wang, and J. Wan, unpublished mapping*, 1997], a fault not imaged by the INDEPTH seismic data. Second, INDEPTH seismic reflections have been interpreted to show a ~35 km high antiformal duplex in the hanging wall of a crustal ramp along the Main Himalayan Thrust (MHT) beneath the core of the Kangmar Dome [*Hauck et al.*, 1998], although *Makovsky et al.* [1999] argue that the MHT maintains a constant dip through this region (Figure 13).

The crux of the problem is that D2 fabrics indicate extensional deformation at midcrustal depths and mica cooling ages suggest underthrusting of a cold slab. Because normal faults that could have accommodated the penetrative D2 extensional deformation were not observed in the Kangmar region, we suggest that the D2 deformation was accommodated by normal slip along the STDS

(a)

Early(?) to Middle Miocene

(b)

Present
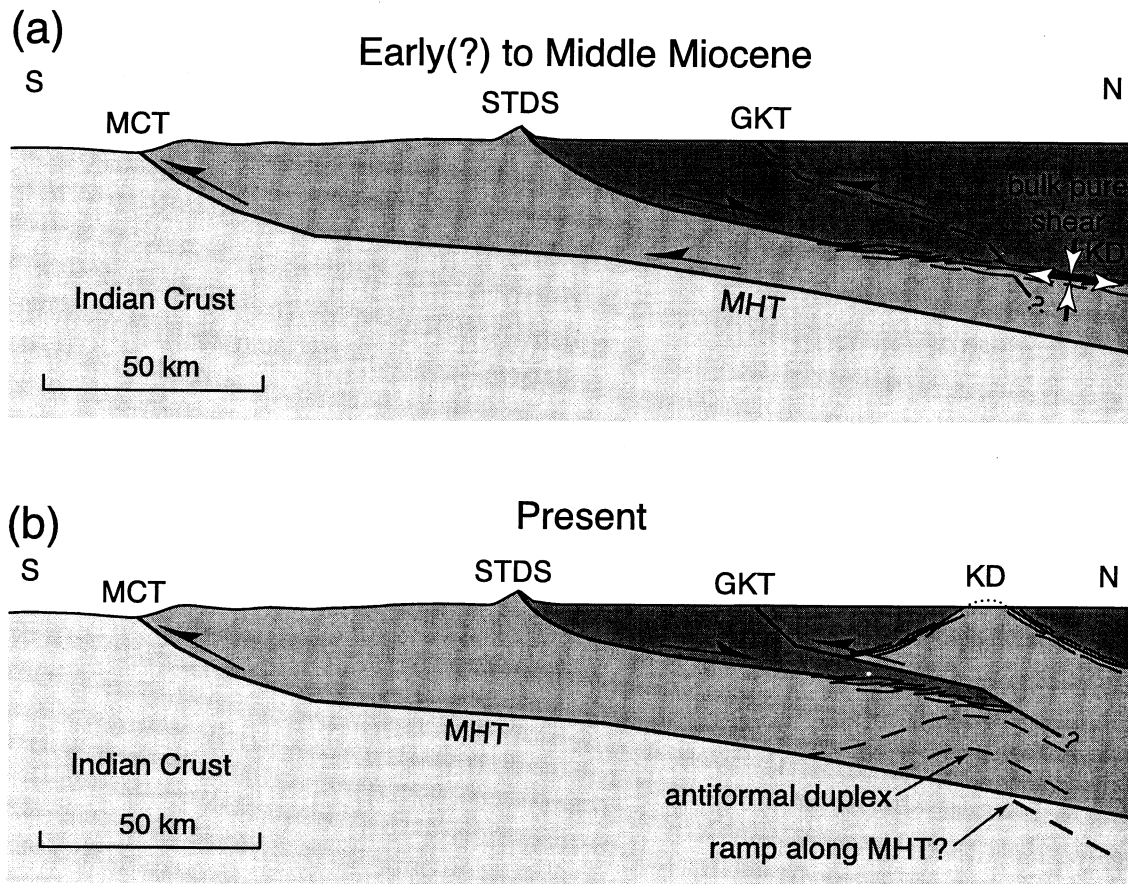
Figure 13. Interpretative, schematic, evolutionary N-S cross sections across the Himalaya and southern Tibet at the longitude of the Kangmar Dome. (a) Configuration of major structures and D2 extensional fabrics in the Kangmar Dome during the early(?) to middle Miocene. (b) Configuration of major structures at present. See text for details. Modified from *Hauck et al.* [1998], *Wu et al.* [1998], and *Makovsky et al.* [1999]. GKT, Gyirong-Kangmar thrust fault system; KD, Kangmar Dome; MCT, Main Central Thrust; MHT, Main Himalayan Thrust; STDS, Southern Tibetan Detachment System.

(Figure 13). In this model, early(?) to middle Miocene normal slip along the STDS merged at depth into a zone of ductile shear that terminated into a root zone of bulk coaxial strain that we observe in the Kangmar Dome (Figure 13a) [cf. *Lister and Davis*, 1989]. Here the rheologically weakened middle crust vertically thinned and horizontally stretched, resulting in the development of the subhorizontal D2 fabrics. Because D2 deformation began during or soon after the peak of metamorphism, which most likely occurred between 40 and 20 Ma (see section 7.3), and kinematic indicators composed of asymmetric tails of recrystallized kspar and growth of biotite and muscovite in strain shadows, temperatures were ~450°-600°C, well in excess of mica $^{40}Ar/^{39}Ar$ closure temperatures, and therefore the timing of D2 deformation is constrained to between 40-20 and ~15 Ma.

Mica cooling ages increase with depth, indicating rapid cooling (25°-70°C) at 15-11 Ma, which we interpret as refrigeration by underthrusting of cold Tethyan sediments. In addition, mica cooling ages young northward within a single structural horizon. We suggest that these relations indicate that the Kangmar rocks were captured in the hanging wall of a north dipping thrust fault, the GKT (Figure 13), and uplifted southward during the middle Miocene. Subsequent movement of these rocks up and over a north dipping ramp along the GKT resulted

in passive doming of the S2 mylonitic foliation, peak metamorphic isobars and isotherms, and mica $^{40}Ar/^{39}Ar$ isochrons. If *Hauck et al.*'s [1998] interpretation that a north dipping ramp with a hanging wall antiformal duplex is present along the MHT beneath the Kangmar Dome is correct, then the north dipping ramp along the GKT may be part of this antiformal duplex. Because mica $^{40}Ar/^{39}Ar$ isochrons are domed and potassium feldspar $^{40}Ar/^{39}Ar$ and apatite fission track isochrons are not, doming occurred at ~11 Ma and at temperatures of 335°-300°C. Symmetric cooling of the dome from ~300° to 120°C between ~11 and 5.5 Ma implies either cessation of thrust faulting and rapid exhumation (~20-40°C/Myr) due to erosion following thrust faulting or continued slip along a subhorizontal portion of the GKT and erosion. Assuming a geothermal gradient of 30°C/km implies an exhumation rate of ~1.0 mm/yr during this period.

7.3. Tectonic Context

The development of D1 south vergent folds is likely related to the initial underthrusting of the Indian Plate beneath its miogeoclinal deposits. The timing of this event is not constrained in this study but has been inferred to be early to

middle Eocene in the Annapurna [*Godin et al.*, 1999; *Hodges et al.*, 1996; *Vannay and Hodges*, 1996] and Ladakh-Zanskar regions [*Searle et al.*, 1988]. Thermal reequilibration following this crustal thickening produced the high-temperature/moderate-pressure metamorphism recorded at Kangmar Dome. Our investigation only constrains the timing of peak metamorphism to between the Carboniferous and ~15 Ma. However, the characteristic time for thermal diffusion through 15-30 km thick crust is 7.5-30 Myr, suggesting that the peak metamorphism occurred between 40 and 20 Ma.

The D2 deformational event occurred after peak metamorphism and prior to mica cooling at ~15 Ma. Because the timing of thrusting along the Gangdese and Renbu-Zedong thrust fault systems to the north is estimated to be late Oligocene to early Miocene and early to late Miocene, respectively [*Yin et al.*, 1994; *Ratschbacher et al.*, 1994; *Quidelleur et al.*, 1997], and initial slip along the MCT is late Oligocene to early Miocene [*Hubbard and Harrison*, 1989; *Harrison et al.*, 1995; *Coleman and Parrish*, 1995], these relations suggest that vertical thinning and horizontal extension in the Kangmar region, accommodated by normal slip along the STDS, was coeval with contractional deformation to the north and south.

The development of subhorizontal tension, leading to normal slip along the STDS and thereby the formation of the D2 extensional fabrics in the Kangmar Dome, has been attributed to either gravitational collapse of overthickened crust or a reduction in the coefficient of friction along the MHT [*Burchfiel and Royden*, 1985; *Royden and Burchfiel*, 1987]. Like *Burchfiel et al.* [1992], we suggest that extension was triggered by the thermally weakened middle crust, a result of conductive relaxation of isotherms following D1 deformation. Because the Mabja and Kangmar domes (Figure 1) exhibit similar deformational and metamorphic histories [*Lee et al.*, 1998], we infer that during the early(?) to middle Miocene much of the middle crust in southern Tibet was thermally hot and weak, and therefore was undergoing horizontal extension and vertical thinning.

Geochronologic studies reveal that slip along the STDS in the Wagye La and Khula Kangri areas (Figure 1), 40-80 km south and southeast of the Kangmar Dome, respectively, was occurring at ~12 Ma [*Edwards and Harrison*, 1997; *Wu et al.*, 1998]. The 15–11 Ma cooling history we have documented in the Kangmar Dome is synchronous with this, implying that normal slip contin-

ued along the STDS while the deformation regime in its root zone switched to contraction. Normal slip along the STDS accompanied by contractional deformation in its hanging wall indicates simultaneous extension and contraction within southern Tibet during the middle Miocene. We speculate that increased friction along the MHT beneath the Kangmar Dome region leads to the change from extension to contraction [e.g., *Dahlen*, 1990].

8. Conclusions

Structural, thermobarometric, and thermochronologic investigations in the Kangmar Dome reveal a deformational and thermal history characterized by N-S contraction, thermal reequilibration leading to moderate-pressure/high-temperature metamorphism, subsequent vertical thinning and horizontal extension, and finally, exhumation by thrust faulting and erosion. These data indicate that the formation of the gneiss dome cannot be attributed to either metamorphic core complex-type extension, diapirism, or duplex formation. Rather, we suggest that the formation of extensional fabrics occurred in a zone of coaxial strain within the root zone of the STDS. We attribute the development of D2 extensional fabrics and normal slip along the STDS to gravitational collapse of overthickened crust or a reduction in the coefficient of friction along the MHT. Subsequent movement up and over a north dipping thrust fault ramp resulted in the domal form. Mica, potassium feldspar, and apatite fission track thermochronology indicate that exhumation of the Kangmar Dome by thrust faulting and erosion occurred during the middle Miocene. Exhumation of the Kangmar Dome is synchronous with normal slip along the STDS and thrust faulting along the Renbu-Zedong thrust fault, indicating that extension and contraction was occurring simultaneously within southern Tibet.

References

Armijo, R., P. Tapponnier, J. Mercier, and T. Han, Quaternary extension in southern Tibet: Field observations and tectonic implications, *J. Geophys. Res., 91*, 13,803-13,872, 1986.

Bohlen, S.R., A. Montana, and D.M. Kerrick, Precise determinations of the equilibria kyanite = sillimanite and kyanite = andalusite and a revised triple point for Al$_2$SiO$_5$ polymorphs, *Am. Mineral., 76*, 677-680, 1991.

Brun, J.-P., L'origine des domes gneissiques: Modeles et tests, *Bull. Soc. Geol. Fr., 25*, 219-228, 1983.

Brun, J.P., and J. Van Den Driessche, Extensional gneiss domes and detachment faults — Structure and kinematics, *Bull. Soc. Geol. Fr., 165*, 519-530, 1994.

Burchfiel, B.C., and L.H. Royden, North-south extension within the convergent Himalayan region, *Geology, 13*, 679-682, 1985.

Burchfiel, B.C., C. Zhiliang, K.V. Hodges, L. Yuping, L.H. Royden, D. Changrong, and X. Jiene, The south Tibetan detachment system, Himalayan orogen: Extension contemporaneous with and

parallel to shortening in a collisional mountain belt, *Spec. Pap. Geol. Soc. Am. 269*, 41 pp., 1992.

Burg, J.P., and J.M. Chen, Tectonics and structural zonation of southern Tibet, China, *Nature, 311*, 219-223, 1984.

Burg, J.P., M. Guiraud, G.M. Chen, and G.C. Li, Himalayan metamorphism and deformations in the north Himalayan Belt (southern Tibet, China), *Earth Planet. Sci. Lett., 69*, 391-400, 1984.

Chen, Z., Y. Liu, K.V. Hodges, B.C. Burchfiel, L.H. Royden, and C. Deng, The Kangmar Dome: A metamorphic core complex in southern Xizang (Tibet), *Science, 250*, 1552-1556, 1990.

Coleman, M.E., and R.R. Parrish, Constraints on Miocene high-temperature deformation and anatexis within the Greater Himalaya from U-Pb geochronology, (abstract), *Eos. Trans. AGU, 76(46)*, Fall Meet. Suppl., F708, 1995.

Dahlen, F.A., Critical taper model of fold-and-thrust belts and accretionary wedges, *Annu. Rev. Earth Planet. Sci., 18*, 55-99, 1990.

Dodson, M.H., Closure temperature in cooling

geochronological and petrological systems, *Contrib. Mineral. Petrol., 40*, 259-274, 1973.

Edwards, M.A., and T.M. Harrison, When did the roof collapse? Late Miocene N-S extension in the high Himalaya revealed by Th-Pb dating of the Khula Kangri granite, *Geology, 25*, 543-546, 1997.

Elkins, L.T., and T.L. Grove, Ternary feldspar experiments and thermodynamic models, *Am. Mineral., 75*, 544-559, 1990.

England, P., and P. Molnar, Cause and effect among thrust faulting and normal faulting, anatectic melting and exhumation in the Himalaya, in *Himalayan Tectonics*, edited by P.J. Treloar and M.P. Searle, *Geol. Soc. Spec. Publ., 74*, 401-411, 1993.

England, P.C., and G. Houseman, Extension during continental convergence with application to the Tibetan Plateau, *J. Geophy. Res., 94*, 17,561-17,579, 1989.

Eskola, P.E., The problem of mantled gneiss domes, *Q. J. Geol. Soc. London, 104*, 461-476, 1949.

Ferry, J.M., and F.S. Spear, Experimental calibration

of the partitioning of Fe and Mg between biotite and garnet, *Contrib. Mineral. Petrol., 66,* 113-117, 1978.

Galbraith, R.F., and G.M. Laslett, Statistical models for mixed fission track ages, *Nucl. Tracks Radiat. Meas., 21,* 459-470, 1993.

Ganguly, J., W. Cheng, and M. Tirone, Thermodynamics of aluminosilicate garnet solid solution: New experimental data, and optimized model, and thermometric applications, *Contrib. Mineral. Petrol., 126,* 137-151, 1996.

Gansser, A., *Geology of the Himalayas,* 289 pp., Wiley-Interscience, New York, 1964.

Ghent, E.D., Plagioclase-garnet-Al$_2$SiO$_5$-quartz: A potential geobarometer-geothermometer, *Am. Mineral., 61,* 710-714, 1976.

Ghent, E.D., and M.Z. Stout, Geobarometry and geothermometry of plagioclase-biotite-garnet-muscovite assemblages, *Contrib. Mineral. Petrol., 76,* 92-97, 1981.

Ghent, E.D., D.B. Robbins, and M.Z. Stout, Geothermometry, geobarometry, and fluid compositions of metamorphosed calc-silicates and pelites, Mica Creek, British Columbia, *Am. Mineral., 64,* 874-885, 1979.

Godin, L., R.L. Brown, S. Hanmer, and R. Parrish, Back folds in the core of the Himalayan orogen: An alternative interpretation, *Geology, 27,* 151-154, 1999.

Grove, M., and T.M. Harrison, ^{40}Ar* diffusion in Fe-rich biotite, *Am. Mineral., 81,* 940-951, 1996.

Hayden, H.H., The geology of the provinces of Tsan and Ü in central Tibet, *Mem. Geol. Surv. India, 36,* 122-198, 1912.

Harrison, T.M., Diffusion of ^{40}Ar in hornblende, *Contrib. Mineral. Petrol., 78,* 324-331, 1981.

Harrison, T.M., I. Ducan, and I. McDougall, Diffusion of ^{40}Ar in biotite — Temperature, pressure and compositional effects, *Geochim. Cosmochim. Acta, 49,* 2461-2468, 1985.

Harrison, T.M., K.D. McKeegan, and P. LeFort, Detection of inherited monazite in the Manaslu leucogranite by ^{208}Th/^{232}Th ion microprobe dating: Crystallization age and tectonic implications, *Earth Planet. Sci. Lett., 133,* 271-282, 1995.

Harrison, T.M., O.M. Lovera, and M. Grove, New insights into the origin of two contrasting Himalayan granite belts, *Geology, 25,* 899-902, 1997.

Hauck, M.L., K.D. Nelson, L.D. Brown, W. Zhao, and A.R. Ross, Crustal structure of the Himalayan orogen at ~90° east longitude from Project INDEPTH deep reflection profiles, *Tectonics, 17,* 481-500, 1998.

Hodges, K.V., and F.S. Spear, Geothermometry, geobarometry and the Al$_2$SiO triple point at Mt Moosilauke, New Hampshire, *Am. Mineral., 67,* 1118-1134, 1982.

Hodges, K.V., R.R. Parrish, T.B. Housh, D.R. Lux, B.C. Burchfiel, L.H. Royden, and Z. Chen, Simultaneous Miocene extension and shortening in the Himalaya orogen, *Science, 258,* 1466-1469, 1992.

Hodges, K.V., R.R. Parrish, and M.P. Searle, Tectonic evolution of the central Annapurna range, Nepalese Himalayas, *Tectonics, 15,* 1264-1291, 1996.

Holland, T. J. B., and R. Powell, An internally consistent thermodynamic data set for phases of petrologic interest, *J. Metamorph. Geol., 16,* 309-343, 1998.

Hubbard, M.S., and T.M. Harrison, ^{40}Ar/^{39}Ar age constraints on deformation and metamorphism in the main central thrust zone and Tibetan slab, eastern Nepal Himalaya, *Tectonics, 8,* 865-880, 1989.

Lee, J., P. Gans, W. McClelland, Y. Wang, and L. Qi, Structural evolution of the Mabja Dome, southern Tibet, (abstract), *Eos Trans. AGU, 79(45),* Fall Meet. Suppl., F794, 1998.

Le Fort, P., Himalayas: The collided range; Present knowledge of the continental arc, *Am. J. Sci., 275-(A),* 1-44, 1975.

Le Fort, P., Metamorphism and magmatism during the Himalayan, in *Collision Tectonics,* edited by M.P. Coward and A.C. Ries, *Geol. Soc. Spec. Publ., 19,* 159-172, 1986.

Le Fort, P., M. Cuney, C. Deniel, C. France-Lanord, S.M.F. Sheppard, B.N. Upreti, and P. Vidal, Crustal generation of the Himalayan leucogranites, *Tectonophysics, 134,* 39-57, 1987.

Liang, D.Y., and W.P. Wang, Discussion of the Carboniferous, Permian systems and their paleobiological groups in Kangma and Lazi Quixia, Tibet, *Contributions to Geology of the Qinghai-Xizang (Tibet) Plateau,* 2, 226 pp., Geological Publishing House, Beijing, 1983.

Lister, G.S., Discussion, Crossed-girdle c-axis fabrics in quartzites plastically deformed by plane strain and progressive simple shear, *Tectonophysics, 39,* 51-54, 1977.

Lister, G.S., and S.L. Baldwin, Modelling the effect of arbitrary P-T-t histories on argon diffusion in minerals using the MacArgon program for the Apple Macintosh, *Tectonophysics, 253,* 83-109, 1996.

Lister, G.S., and G.A. Davis, The origin of metamorphic core complexes and detachment faults formed during Tertiary continental extension in the northern Colorado River region, U.S.A., *J. Struct. Geol., 11,* 65-94, 1989.

Lister, G.S., and B.E. Hobbs, The simulation of fabric development during plastic deformation and its application to quartzite: The influence of deformation history, *J. Struct. Geol., 2,* 355-370, 1980.

Lovera, O.M., F.M. Richter, and T.M. Harrison, ^{40}Ar/^{39}Ar thermochronology for slowly cooled samples having a distribution of diffusion domain sizes, *J. Geophys. Res., 94,* 17,917-17,936, 1989.

Makovsky, Y., S.L. Klemperer, L. Ratschbacher, and D. Alsdorf, Midcrustal reflector on INDEPTH wide angle profiles: An ophiolitic slab beneath the India-Asia suture in southern Tibet?, *Tectonics, 18,* 793-808, 1999.

Maluski, H., P. Matte, and M. Brunel, Argon 39-Argon 40 dating of metamorphic and plutonic events in the north and high Himalayas belts (southern Tibet-China), *Tectonics, 7,* 299-326, 1988.

Miller, E.L., A.T. Calvert, and T.A. Little, Strain-collapsed metamorphic isograds in a sillimanite gneiss dome, Seward Peninsular, Alaska, *Geology, 20,* 487-490, 1992.

Molnar, P., and H. Lyon-Caen, Fault plane solutions of earthquakes and active tectonics of the Tibetan plateau and its margins, *Geophys. J. Int., 99,* 123-153, 1989.

Molnar, P., and P. Tapponnier, Effects of a continental collision, *Science, 189,* 419-426, 1975.

Molnar, P., and P. Tapponnier, Active tectonics of Tibet, *J. Geophys. Res., 83,* 5361-5375, 1978.

Naeser, C. W., *Fission Track Dating, U.S. Geol. Surv. Open File Rep. 76-190,* 1-65, 1976.

Naeser, C. W., Fission-track dating and geologic annealing of fission tracks, in *Lectures in Isotope Geology,* edited by E. Jäger, and J. C. Hunziker, pp. 154-169, Springer-Verlag, New York, 1979.

Pan, Y., and W.S.F. Kidd, Nyainqentanglha shear zone: A late Miocene extensional detachment in the southern Tibetan Plateau, *Geology, 20,* 775-778, 1992.

Passchier, C.W., and C. Simpson, Porphyroclast systems as kinematic indicators, *J. Struct. Geol., 8,* 831-844, 1986.

Quidelleur, X., M. Grove, O.M. Lovera, T.M. Harrison, A. Yin, and F.J. Ryerson, The thermal evolution and slip history of the Renbu Zedong thrust, southeastern Tibet, *J. Geophy. Res., 102,* 2659-2679, 1997.

Ramberg, H., Diapirism and gravity collapse in the Scandinavian Caledonides, *J. Geol. Soc. London, 137,* 261-270, 1980.

Ramsay, J.G., *Folding and Fracturing of Rocks,* 568 pp., McGraw-Hill, New York, 1967.

Ratschbacher, L., W. Frisch, G. Liu, and C. Chen,

Distributed deformation in southern and western Tibet during and after the India-Asia collision, *J. Geophy. Res., 99,* 19,917-19,945, 1994.

Royden, L.H., and B.C. Burchfiel, Thin-skinned north-south extension within the convergent Himalayan region: Gravitational collapse of a Miocene topographic front, in *Continental Extensional Tectonics,* edited by M.P. Coward, J.F. Dewey, and P.L. Hancock, *Geol. Soc. Spec. Publ., 28,* 611-619, 1987.

Sanderson, D.J., The development of fold axes oblique to the regional trend, *Tectonophysics, 16,* 55-70, 1973.

Schärer, U., R. Xu, and C. Allegre, U-(Th)-Pb systematics and ages of Himalayan leucogranites, south Tibet, *Earth Planet. Sci. Lett., 77,* 35-48, 1986.

Searle, M.P., Stratigraphy, structure and evolution of the Tibetan-Tethys zone in Zanskar and the Indus suture zone in the Ladakh Himalaya, *Trans. R. Soc. Edinburgh Earth Sci., 73,* 205-219, 1983.

Searle, M.P., D.J.W. Cooper, and A.J. Rex, Collision tectonics of the Ladakh Zanskar Himalaya, *Philos. Trans. R. Soc. London, Ser. A, 326,* 117-150, 1988.

Stacey, J.S., and J.D. Kramers, Approximation of terrestrial lead isotope evolution by a two-stage model, *Earth Planet. Sci. Lett., 26,* 207-221, 1975.

Tapponnier, P., G. Peltzer, A.Y. Le Dain, R. Armijo, and P. Cobbold, Propagating extrusion tectonics in Asia: New insights from simple experiments from plasticine, *Geology, 10,* 611-615, 1982.

Thompson, A.B., and P.C. England, Pressure-temperature-time paths of regional metamorphism, II: Their influence and interpretation using mineral assemblages in metamorphic rocks, *J. Petrol., 25,* 929-955, 1984.

Vannay, J.-C., and K.V. Hodges, Tectonomorphic evolution of the Himalayan metamorphic core between the Annapurna and Dhaulagiri, central Nepal, *J. Metamorph. Geol., 14,* 635-656, 1996.

Wu, C., K.D. Nelson, G. Wortman, S.D. Samson, Y. Yue, J. Li, W.S.F. Kidd, and M.A. Edwards, Yadong cross structure and south Tibetan detachment in the east central Himalaya (89°-90°E), *Tectonics, 17,* 28-45, 1998.

Yin, A., T.M. Harrison, F.J. Ryerson, W. Chen, W.S.F. Kidd, and P. Copeland, Tertiary structural evolution of the Gangdese thrust system, southeastern Tibet, *J. Geophys. Res., 99,* 18,175-18,201, 1994.

Zhang, Q., Y.S. Zhou, D.Z. Li, and H.R. Wu, Principal features of the gneissic dome and its peripheral metamorphic zones in Kangma of Xizang, China, *Sci. Geol. Sin., 2,* 125-133, 1986.

Zhou, Y.S., Q. Zhang, C.W. Jin, and H.J. Mei, *Magmatism and Metamorphism in Xizang (Tibet): The Series of the Scientific Expedition to Qinghai-Xizang,* 359 pp., Sci. Press, Beijing, 1981.

A.E. Blythe, Department of Earth Sciences, University of Southern California, Los Angeles, CA 90089. (blythe@earth.usc.edu)

A. Calvert, P. Gans, and B.R. Hacker, Department of Geological Sciences, University of California, Santa Barbara, CA 93106. (calvert@geol.ucsb.edu; gans@geol.ucsb.edu; hacker@geol.ucsb.edu)

W.S. Dinklage, Geology Department, Wittenberg University, Springfield, OH 45501. (wdinklage@wittenberg.edu)

J. Lee, Department of Geological Sciences, Central Washington University, 400 East 8th Avenue, Ellensburg, WA 98926. (jeff@geology.cwu.edu)

W. McClelland, Department of Geological Sciences, University of Idaho, Moscow, ID 83844. (billm@iron.mines.uidaho.edu)

J.L. Wan and Y. Wang, Institute of Geology, State Seismological Bureau, Beijing 100029, China.

Plate 1. Simplified geologic map of the Kangmar Dome.

Plate 2. Interpretative N-S cross section of the Kangmar Dome. See Plate 1 for location.